

# Characteristics of tropical and subtropical atmospheric moistening derived from Lagrangian mass balance constrained by measurements of HDO and H<sub>2</sub>O

Derek Brown,<sup>1</sup> John Worden,<sup>2</sup> and David Noone<sup>1</sup>

Received July 17 2012; revised November 11 2012; accepted November 13 2012.

[1] Regional tropospheric water balance depends on local mixing rates, moistening and precipitation efficiency associated with cloud processes, and large-scale moisture advection. Conventional data sets are insufficient to disentangle how these processes affect the regional humidity, and models are limited by their need to parameterize many of the pertinent mechanisms, including precipitation efficiency, evaporation of cloud condensate, and mixing rates. This study provides new insight by constraining a Lagrangian mass balance model with satellite measurements of specific humidity and the HDO/H<sub>2</sub>O ratio in water vapor. Seasonal estimates of mixing rates, moistening efficiency, isotopic composition of source waters, and effective isotopic fractionation in clouds are calculated. Analysis shows that the water source is dominated by cloud evaporation in the dry subtropics, subcloud rainfall recycling in the humid subtropics, and convective detrainment and postcondensational exchange during tropical monsoons. Moistening efficiency is shown to be as twice as strong over the wintertime subtropics as over other regions. Over monsoonal areas, however, moistening efficiency decreases during times of most intense mixing, since postcondensational exchange and convective recycling effects act to dehydrate and isotopically deplete the local water sources. A robust relationship is found between precipitation efficiency derived from rainfall profile measurements and differences in effective and equilibrium isotopic fractionation rates, suggesting that isotopic observations might enable estimates of this illusive parameter to be inferred directly. In spite of the simple modeling framework employed, the results provide insight in to the gains that can be expected by assimilating satellite observations of isotope ratios into more comprehensive, isotope-enabled general circulation models.

**Citation:** Brown, D., J. Worden, D. Noone (2013), Characteristics of tropical and subtropical atmospheric moistening derived from Lagrangian mass balance constrained by measurements of HDO and H<sub>2</sub>O, *J. Geophys. Res.*, 118, doi:10.1029/2012JD018507

## 1. Introduction

[2] The distribution of moistening processes over different regions is important for atmospheric water and energy balances, yet difficulties remain in understanding and accurately representing the strength and variability of the contributing components. For instance, strong seasonal variability in the balance of moistening from horizontal transport, vertical convective transport, and condensate evaporation over the Amazon emerge in atmospheric

reanalysis data [Fu *et al.*, 1999]. The relative strength of each component in such a system is difficult to ascertain, since modeling studies have shown limitations in accurately simulating the strength and variability of regional convection and have also exposed shortcomings in the bulk representation of cloud processes [e.g., Mapes *et al.*, 2009; Wright *et al.*, 2009a]. In addition, debate remains on whether cross isentropic exchange of water is associated primarily with dynamic processes (large scale or convective scale) [Yang and Pierrehumbert, 1994] or with condensate evaporation [e.g., Sun and Lindzen, 1993; Couhert *et al.*, 2010]. This study's purpose is to increase the understanding of these moistening complexities by testing the relationship between the water balance of the atmosphere and the moistening mechanisms that predominate in different regions in the tropics and subtropics. This is achieved using HDO/H<sub>2</sub>O ratios in water vapor, which capture information about the processes that hydrate and dehydrate the atmosphere.

[3] Differentiating between various moistening and dehydration processes is made possible primarily by two unique aspects of isotope ratios found in water vapor. First,

<sup>1</sup>Department of Atmospheric and Oceanic Sciences, and Cooperative Institute for Research in Environmental Sciences, University of Colorado, Boulder, Colorado, USA.

<sup>2</sup>Jet Propulsion Laboratory, California Institute of Technology, Pasadena, California, USA.

Corresponding author: D. Brown, Department of Atmospheric and Oceanic Sciences, and Cooperative Institute for Research in Environmental Sciences, University of Colorado, Boulder, Colorado 80309. (Derek.Brown@colorado.edu)

isotopic fractionation occurs during phase changes since, at equilibrium, the lower saturation vapor pressure of HDO compared with that of H<sub>2</sub>O results in a higher relative concentration of the heavy isotopes (HDO) in the condensed phase [Dansgaard, 1964; Craig and Gordon, 1965]. Second, the isotopologues of water are fractionated as a result of differing rates of diffusive transport during evaporation and condensation events [Craig and Gordon, 1965; Jouzel and Merlivat, 1984; Cappa et al., 2003]. Both of these fractionation mechanisms introduce variability in the distribution of isotopic ratios in water vapor. Thus, observations of the HDO/H<sub>2</sub>O isotope ratio in water vapor provide insight into the history of moisture exchanges, which complements measurements of water amount. Isotope ratio information can be used to provide a more complete assessment of the components that act to balance moistening in different geographic regions.

[4] Isotope ratios in water vapor have been shown to be sensitive to changes in the nature and strength of convection [Lawrence and Gedzelman, 1996; 2003; Gedzelman et al., 2003; Lawrence et al., 2004], changes in air mass origin [Galewsky and Hurley, 2010; Noone et al., 2011], cloud microphysical processes [Merlivat and Jouzel, 1979; Noone, 2012], and rainfall re-evaporation [Worden et al., 2007; Bony et al., 2008; Risi et al., 2012a; 2012b]. To this effect, observed D/H ratios have been used alongside simple models to provide important fingerprints of atmospheric processes [Zakharov et al., 2004; Herbin et al., 2007; Payne et al., 2007; Worden et al., 2007; Brown et al., 2008; Noone, 2008] that are difficult to ascertain using water vapor measurements alone.

[5] To interpret isotopic data properly, however, a firm understanding of the numerous controls on isotope ratios is needed. Although the description of isotope ratios as following a Rayleigh processes [Dansgaard, 1964] is intuitively useful, it has significant limitations when applied to many real-world cases. For example, shortcomings arise from a lack of accounting for air mass mixing (including surface water fluxes) and from problems with correctly specifying detailed cloud physics [Hendricks et al., 2000; Worden et al., 2007; Brown et al., 2008; Noone, 2008]. The effects of air mass mixing also introduce non-Rayleigh isotopic variability of the residual vapor [Webster and Heymsfield, 2003; Lawrence et al., 2004; Schmidt et al., 2005; Worden et al., 2007; Brown et al., 2008; Wright et al., 2009b; Field et al., 2010]. Although isotope-enabled general circulation models (GCMs) parameterize many of these processes [Noone and Sturm, 2010], it remains a challenge to reproduce the increasing number of isotope ratio observations. For example, Angert et al. [2008] revealed that variability in vertical transport over the eastern Mediterranean primarily dictated the seasonality of the observed isotopic distributions of water vapor, which was not reproduced by an isotope-enabled GCM. Indeed, Risi et al. [2012a; 2012b] compared satellite-derived estimates of HDO/H<sub>2</sub>O ratios with a set of GCM simulations to identify specific shortcomings in model representation of atmospheric water budgets, which highlights the value of using processes that are identified specifically by isotopic observations to improve models.

[6] Isotopic signatures in vapor are sensitive to the degree of cloud evaporation, since reversible moist adiabatic processes and evaporating clouds lead to higher isotope ratios than processes in which all condensate is instantaneously removed

from the system (i.e., a Rayleigh model) [Merlivat and Jouzel, 1979; Noone, 2012]. Modeling studies suggest that evaporating cumuli moisten subsiding air at atmospheric levels below 500 hPa [Gamache and Houze, 1983; Betts, 1990; Sun and Lindzen, 1993]. Notably, however, advection – condensation models [e.g., Sherwood, 1996; Pierrehumbert, 1998; Galewsky et al., 2005; Galewsky and Hurley, 2010; Hurley and Galewsky, 2010], which are widely used to describe subtropical water vapor distributions, broadly neglect this rehydrating effect, because it is likely to occur during last saturation [Sherwood et al., 2010]. Cloud evaporation is related to the precipitation efficiency (defined here as the fraction of cloud water that is ultimately removed as precipitation), which is a quantity with important effects on tropical humidity [Bony and Emanuel, 2005], tropical cirrus formation, and the associated radiative balance [Lindzen et al., 2001].

[7] Aside from cloud evaporation, intense convection can lead to moisture recycling. The isotopic fingerprint of moisture recycling during intense convection has been found, in studies using models [Risi et al., 2008; Wright et al., 2009b; Field et al., 2010] and observations [Worden et al., 2007; Lee et al., 2011], to be related to additional depletion of residual vapor following condensation because of isotopic exchange with, or evaporation of, precipitation (i.e., postcondensational isotopic exchange). Additionally, Risi et al. [2008] used a one-dimensional model to show that this residual and depleted vapor can become incorporated into the subcloud layer by convective mixing with unsaturated downdrafts, which can subsequently lead to an “amount effect” (i.e., isotopic depletion of precipitation beyond Rayleigh distillation expectations [Dansgaard, 1964; Rozanski et al., 1992; Araguas-Araguas et al., 1998]) in the storm’s precipitation after the reintroduction of the subcloud vapor into the storm. The amount effect is well-documented in ice cores near monsoonal regions [Wushiki, 1977; Grootes et al., 1989], and confirmation of its mechanistic roots using observations is thus warranted.

[8] By merging measurements of water vapor and HDO/H<sub>2</sub>O ratios from the NASA Tropospheric Emission Spectrometer (TES) with a Lagrangian mass balance model, this study evaluates the relationships between dehydration and moistening processes that are associated with clouds, air mass mixing, and moisture recycling. The analysis focuses primarily on interpreting quantities that arise uniquely from the isotopic constraints. These are the HDO/H<sub>2</sub>O ratios of the regional water vapor pools (hereafter “source vapor”) that mix with overlying air parcels and the bulk effective fractionation associated with clouds. We find that, in cloudy regions, convective mixing strength, moistening efficiency (defined here as fractional increases in tropospheric humidity resulting from local moistening), and bulk isotopic fractionation are related to the degree to which water vapor is recycled. This result allows a test of the predictions from global scale models on the origin of the isotopic amount effect by associating observations of anomalously low isotope ratios in water vapor with intense convection and moisture recycling. We also find significant correlations between our modeled effective isotopic fractionation rates and precipitation efficiency values and thus provide confidence for future modeling work aimed at using isotopic methods to expose atmospheric moistening via cloud evaporation.

[9] The following section describes the TES data, the Lagrangian model, and the method by which the two are

merged. A comparison between the model water balance and an atmospheric Reanalysis is shown to provide confidence in the calculation. The results in section 3 use isotopic information to quantify and compare atmospheric mixing time scales, moistening efficiency, precipitation efficiency, and effective isotopic fractionation occurring during cloud processes in different geographic regions throughout the tropics and subtropics. Final remarks and conclusions are presented in the last section.

## 2. Methods and Data

### 2.1. TES Data and Data Quality Control

[10] TES on the NASA *Aura* spacecraft provides estimates of specific humidity and HDO/H<sub>2</sub>O ratios in the midtroposphere. Version 3 data from the TES nadir mode are used, which observes the atmosphere with a footprint of approximately 5.3 by 8.3 km with near-global coverage. The sensitivity of the measurement to the true state is represented by the degrees of freedom. Profiles that are flagged as high quality and that have greater than 0.5 degrees of freedom are selected to ensure that only physically meaningful retrievals are used for analysis [Worden *et al.*, 2007]. The TES HDO/H<sub>2</sub>O ratio estimates have peak sensitivity near 700 hPa under clear sky conditions and near 450 hPa in areas with precipitating cloud [Lee *et al.*, 2011]. Sensitivity decreases with increasing latitude through its dependence on temperature and specific humidity [Worden *et al.*, 2006]. The precision of the H<sub>2</sub>O estimates is ~20%, with a bias in humidity of ~5% for the 500 – 825 hPa atmospheric layer [Clough *et al.*, 2006]. The precision of ~15‰ on the tropospheric HDO/H<sub>2</sub>O ratio is made possible with a joint retrieval algorithm that allows partial cancellation of systematic errors common to both HDO and H<sub>2</sub>O isotopologues [Worden *et al.*, 2006]. A high bias of ~5% in the HDO/H<sub>2</sub>O ratios was identified through comparison with in situ measurements from a laser spectrometer [Worden *et al.*, 2011] and is accounted for in this study; however, uncertainty of ~1% in this bias remains in the absolute values of TES isotope ratios because this bias estimate was formed from a single calibration campaign. Therefore, calculations in this study are made only from differences between nearby TES measurements, reducing the need for absolute measurement accuracy.

[11] Average specific humidity [ $q$ , (g/kg)] and HDO/H<sub>2</sub>O values ( $R$ ) are found at the TES observation locations using mass-weighted averages for the 500 – 825 hPa layer. HDO/H<sub>2</sub>O ratios are presented in “delta” notation, in which

$$\delta D(^0/_{00}) = \left[ \frac{R}{2 \cdot (D/H)_{VSMOW}} - 1 \right] \cdot 1000, \quad (1)$$

and the ratio  $(D/H)_{VSMOW}$  is the Vienna Standard Mean Ocean Water standard for D/H and is  $155.76 \times 10^{-6}$ .

### 2.2. Back Trajectory Data Connections

[12] To constrain a Lagrangian budget calculation (see section 2.3), a search is made to find pairs of observations that are connected via back-trajectories. The back-trajectory model [Noone and Simmonds, 1999; Brown *et al.*, 2008] was run from each TES observation location from September 2004 to March 2008 (888,158 individual observations, using both Special Observation and Global Survey data). Global Survey data are from routine TES observations and provide near-

global coverage, whereas Special Observation data include data taken with higher spatial sampling but over restricted domains, including data from regionally specific validation and research campaigns (<http://tes.jpl.nasa.gov/instrument/globalsurvey/>).

[13] The back-trajectory model uses three-dimensional wind fields from NCAR/NCEP reanalysis data [Kalnay *et al.*, 1996] and assumes an arrival height of 662.5 hPa (nominally in the center of the 500 – 825 hPa layer). Along the 1 – 3 day portions of the back-trajectories, TES observations that occur within 90 minutes and within a circle of radius 120 km are found (hereafter “crossings”). The values of  $q$  and  $R$  at these crossings are calculated by using mass weighting over a 325-hPa-thick layer that is centered at the parcel pressure level. The result is 173,788 1 – 3 day back-trajectories with endpoints in three-dimensional space containing mass weighted  $q$  and  $\delta D$  values found for a 325-hPa-thick layer. Among these, 28,289 trajectories are found in December February (DJF), and 75,885 trajectories are found during June – August (JJA). The  $q$  and  $\delta D$  observations at the endpoints of these trajectories are those used in this study, and these observations all occur within the 2004 – 2008 time period that is spanned by the version 3 TES product. The higher density of JJA trajectories is a result of more Special Observation data during scientific campaigns over the Northern Hemisphere during summer. A test eliminating the Special Observation data yielded results approximately identical to those shown below; however, ultimately the Special Observation data proved useful for reducing uncertainties in modeled values north of 18°N during JJA.

[14] Although short, the 2004 – 2008 period is representative of the 1980 – 2010 climatology, with an overall slight bias toward La Niña conditions and approximately yearly oscillations between relatively weak La Niña and El Niño events during the period. This average bias is found from NOAA/NCEP Atlas data (<http://www.esrl.noaa.gov/psd/cgi-bin/data/composites/printpage.pl>), which shows the period 2004 – 2008 as having slightly higher sea surface temperatures in the Western Equatorial Pacific and slightly lower sea surface temperatures in the Eastern Equatorial Pacific during both JJA and DJF compared with the 1980 – 2010 averages (<0.5 K difference for each region). The Multivariate ENSO index (<http://www.esrl.noaa.gov/psd/ens/mei/>) shows the variability in ENSO phases: weak El Niño conditions exist in 2004, 2005, and 2007; weak La Niña conditions exist in 2006; and stronger La Niña conditions exist in 2008. The average atmospheric conditions during the 2004 – 2008 period show slightly lower temperatures (~0.5 K) and slightly lower precipitable water values (~1 mm) than the 1980 – 2010 average over the Eastern Equatorial Pacific, with concurrent higher temperature (~0.5 K) and precipitable values (~1 mm) over the Pacific Warm Pool. Coupled with these anomalies is a weak extratropical Rossby wave response, which enhances horizontal convergence to the Central Equatorial Pacific. These differences should be borne in mind when considering the results below as representative of the longer climatology.

### 2.3. Lagrangian Mass Transport Model

[15] A parcel mass balance model is developed to capture moisture exchanges between air parcels and local moisture sources, which exposes the effects that convection and



turbulent mixing have on the parcel mixing ratio and isotope ratio. The water vapor mixing ratio and isotope ratio are considered to change via condensation or via the addition of water mass from a source. Because this model accounts for mixing processes *en route*, it differs from pure advection-condensation models, which have been used extensively for water vapor studies [e.g., Sherwood, 1996; Pierrehumbert, 1998; Galewsky *et al.*, 2005; Galewsky and Hurley, 2010; Hurley and Galewsky, 2010]. The H<sub>2</sub>O mass mixing ratio ( $q$ ) along some trajectory evolves as

$$\frac{dq}{dt} = Gq - Lq = k(q_s - q) - aq, \quad (2)$$

where  $G_q$  [(g/kg)/day] is the gain of water vapor per day into the parcel (i.e., the moistening rate) from a nearby moisture reservoir with a specific humidity value,  $q_s$  (g/kg), and  $L_q$  [(g/kg)/day] is the loss of water vapor per day from the parcel (i.e., the condensation rate). Finite changes between the trajectory endpoints (i.e.,  $\Delta q$  over a trajectory of  $\Delta t$  duration in days) are of ultimate concern. The calculation of moisture gain is described by two-member mixing, whereas the linear form for moisture loss is similar to Rayleigh distillation. The rate of moistening and condensation, given by the exchange parameters  $k$  and  $a$  (in units of days<sup>-1</sup>), and the source specific humidity parameter,  $q_s$ , are free parameters.

[16] For the HDO isotopologue, it is convenient to construct the budget in terms of the HDO mass mixing ratio ( $x = \gamma Rq$ , where  $R = [\text{HDO}]/[\text{H}_2\text{O}]$  and  $\gamma$  is the ratio of molecular weights of the two species [i.e.,  $\gamma = 18/19$ ]), as

$$\frac{dx}{dt} = G_x - L_x = \mu k(x_s - x) - \alpha x, \quad (3)$$

where the terms  $G_x$  and  $L_x$  are the rate of supply of HDO from the source to the parcel and the loss of HDO from the parcel via condensation, respectively. The factor  $\mu$  accounts for differing mixing rates for different isotopologues and is taken as  $\mu = 1$ , as is appropriate for purely turbulent exchange [Merlivat and Jouzel, 1979]. Equation 3 contains two additional free parameters, the amount of HDO at the source ( $x_s$ ) and the effective isotopic fractionation during condensation ( $\alpha$ ). The budget for water is closed following the selection of  $a$ ,  $k$ , and  $q_s$ , whereas the isotope budget additionally requires selection of  $\alpha$  and  $x_s$ . The isotope ratio of the moisture sources and the effective fractionation rates offer new information unavailable from specific humidity alone.

[17] The continuous and linear form of equation 2 allows integration between some initial ( $q_0$ ) and final ( $q_{\text{mod}}$ ) points along a Lagrangian trajectory path of duration  $\Delta t$ , and yields the solution

$$q_{\text{mod}} = q_0 \hat{e} + (1 - \hat{e}) \hat{q} \quad (4)$$

where  $\hat{q} = kq_s/(k + a)$  and  $\hat{e} = \exp[-(k + a)\Delta t]$ . In equation 4,  $q_0$  is the specific humidity at the upstream TES observation, and  $q_{\text{mod}}$  is the final modeled value of specific humidity at the downstream endpoint of the trajectory. Similarly, integrating equation 3 along the trajectory path, the isotopic model has the solution

$$x_{\text{mod}} = x_0 \hat{e}_x + (1 - \hat{e}_x) \hat{x} \quad (5)$$

where  $\hat{x} = k\mu x_s/(k\mu + \alpha)$  and  $\hat{e}_x = \exp[-(k\mu + \alpha)\Delta t]$ ,  $x_0$  is the  $x$  value at the trajectory point upstream, whereas  $x_{\text{mod}}$

is the  $x$  value modeled at the downstream endpoint of the trajectory, which is similar to the case for  $q_{\text{mod}}$ .

[18] For any single trajectory, there are only two measurable quantities (the change in  $q$  and the change in  $x$  along the trajectory, i.e.,  $\Delta q/\Delta t$  and  $\Delta x/\Delta t$ ), and, as such, the problem is unconstrained and insoluble for single trajectories. However, the seasonal water and isotopic budgets can be estimated for a given region using an ensemble of individual observations to constrain the model in an ensemble mean sense. We adopt an ensemble approach to estimate seasonal mean values of  $a$ ,  $k$ ,  $q_s$ ,  $\alpha$ , and  $x_s$ .

[19] Estimating the model parameters is written as a minimization of the mismatch between downstream observed values ( $q_{\text{obs}}$  and  $R_{\text{obs}}$ ) and the modeled values ( $q_{\text{mod}}$  and  $R_{\text{mod}}$ ), given the observed upstream values of  $q$  and  $R$  to initialize the model given by equations 4 and 5. A cost function is defined as

$$J = \sqrt{\frac{\sum_{\text{obs}} \Theta^2 \left\{ f \left[ \frac{q_{\text{mod}} - q_{\text{obs}}}{q_{\text{obs}}} \right]^2 + (1 - f) \left[ \frac{R_{\text{mod}} - R_{\text{obs}}}{R_{\text{obs}}} \right]^2 \right\}}{\sum_{\text{obs}} \Theta^2}}, \quad (6)$$

which is minimized by making an optimal selection of the five model parameters. The value of  $f$  determines the relative importance of  $q$  and  $R$  and is chosen here as 0.5 in order to give equal importance to moisture and HDO/H<sub>2</sub>O variability observed within the ensemble. Estimation of the parameters requires appropriate mass weighting to evaluate properly the seasonal, mass-weighted mean water balance (see Appendix A for discussion of the weighting), which requires that the cost function include mass weighting by the average value of  $q$  for each individual trajectory ( $\Theta$ ). Note that it is within the use of the modeled values that the five free model parameters appear. Minimization of the cost function,  $J$ , proceeds through iterative sequential application of the *Brent* [1972] method in five dimensions.

[20] The budgets are evaluated at each point on a 5° latitude by 5° longitude grid over the domain 0°E – 360°E and 40°S – 40°N. For each grid point, all trajectories that arrive within 600 km of the center of the grid point in each season (JJA or DJF) are used to estimate the grid point parameters. Given the estimated set of five free parameters, a unique solution requires at least five individual trajectories in a given region. The choice of a 600 km radius yields 90% of the grid points having between 19 and 334 trajectories, with a mean of 99 trajectories at each grid point. Results calculated from grid points having less than 10 trajectories were omitted from this study because low degrees of freedom cast doubt on these solutions. A single grid point example of arriving trajectories, and their individual  $\Delta q/\Delta t$  and  $\Delta \delta D/\Delta t$  values, is shown in Figure 1.

[21] The choice of a linear model (equations 2 and 3) ensures that the cost function is smooth and uniquely constrains the five free parameters in the model regardless of the initial guesses. This is not the case if, for instance, a nonlinear form is taken for precipitation. The cost function values at the solution point (i.e., minimum) is a measure of the degree to which the individual  $q$  and  $R$  values vary from the modeled mean values. Figure 2 shows the tropical regions generally showing low cost function minima, with the lowest values occurring over the monsoonal regions. This is consistent with

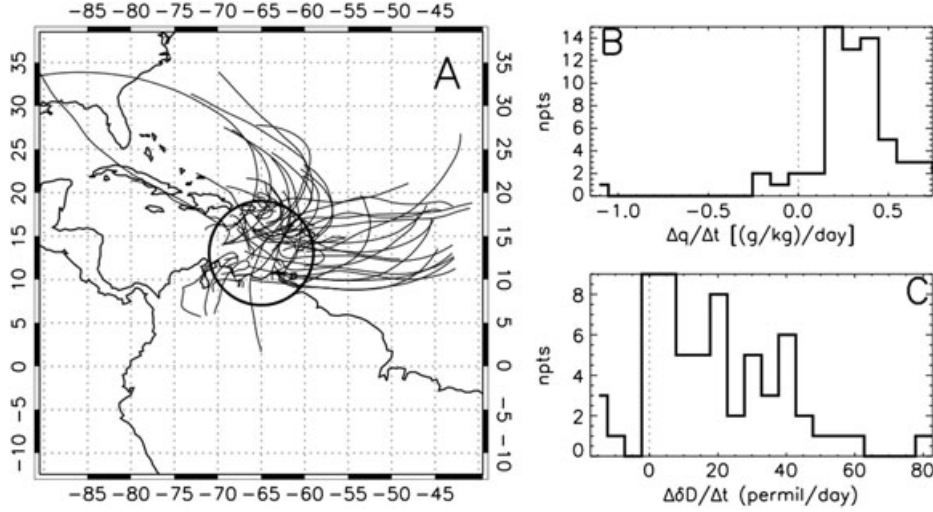


**Figure 1.** Example of individual December-January-February trajectories used to constrain the Lagrangian model for one grid point (A), with histograms of the changes in  $q$  (B) and  $\delta D$  (C) en route.

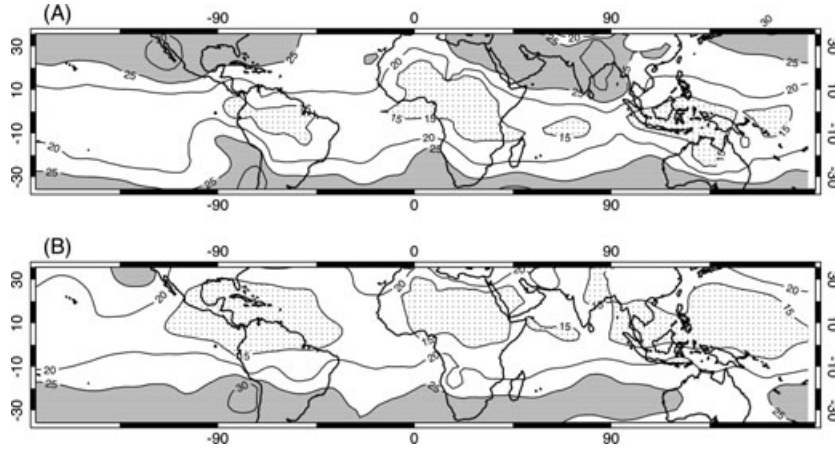


**Figure 2.** Cost function minima (%) for DJF (A) and JJA (B). Areas with the cost function minimum values exceeding 25% are shaded, whereas areas with values below 15% are stippled.

a seasonal surge of tropical moisture that reduces variance among the trajectories. On the other hand, the highly baroclinic midlatitude regions show relatively higher cost function minima. This likely is a result of synoptic-scale disturbances introducing variability in moisture and isotopic composition changes among the intraseasonal trajectories. Our analysis thus highlights those regions (i.e., the tropics and subtropics) where the seasonal estimates are better constrained.

[22] Perturbation tests show that the moisture source specific humidity and isotopic ratio are more strongly constrained than the other parameters. The tropical land regions exhibit the highest sensitivity of the cost function with respect to all parameters and are thus the most well-constrained regions for this model. The least constrained regions are over ocean in the midlatitudes.

### 3. Results

#### 3.1. Changes in Moisture along Trajectories

[23] Figure 3 shows the mean Lagrangian changes in moisture [ $\Delta q/\Delta t$  in units of (g/kg) · day<sup>-1</sup>] derived from

trajectory crossings, which are identical to  $G-L$  values calculated a posteriori using the estimated parameters. In broad terms, moisture losses tend to occur over the monsoonal regions, whereas moisture gains occur primarily in the subtropics. Zonal mean  $\Delta q/\Delta t$  values derived from the (TES) trajectory budget (Fig. 4) are for the most part higher than the two processed NCEP data sets, with generally better agreement during JJA. The better general agreement during JJA likely is related to the increased number of trajectories available during Northern Hemisphere JJA from increased summertime science campaigns (i.e., Special Observation data). The best agreements are from 0°S to 10°S and from 18°N to 30°N during JJA and from 13°N to 40°N during DJF. With combined JJA and DJF seasonal data for the 500 – 825 hPa layer, a map correlation calculation between the mapped trajectory  $\Delta q/\Delta t$  values (i.e., data in Fig. 3) and gridded NCEP-NCAR Reanalysis seasonal moisture flux convergence (hereafter MFC) values yields a map correlation coefficient of 0.73 and a normalized root mean square difference (NRMSD) of 9.8%. A map correlation calculation using mapped trajectory  $\Delta q/\Delta t$  values and mapped values

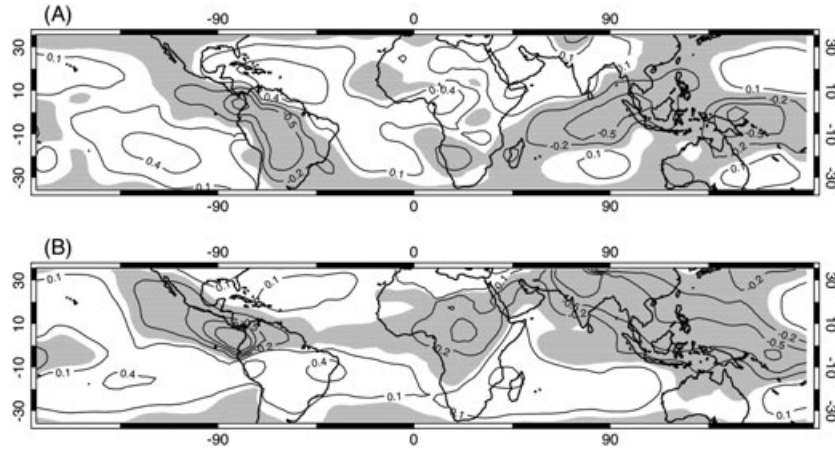


**Figure 3.** Average rate of change in specific humidity for the set of trajectories arriving at each grid point for DJF (A) and JJA (B). Line contour interval is  $0.3 \text{ g} \cdot \text{kg}^{-1} \cdot \text{day}^{-1}$ . Shading indicates negative values.

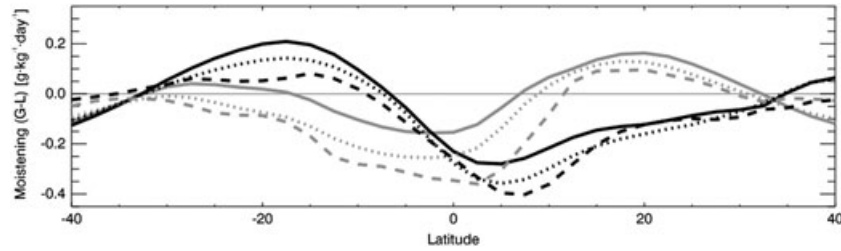


**Figure 4.** Zonal mean model  $G-L$  values (solid), 500 – 825 hPa net convergence values from the NCAR/NCEP Reanalysis (dashed), and NCAR/NCEP Reanalysis  $\Delta q/\Delta t$  (collocated with TES retrievals; dotted) during DJF (gray) and JJA (black).

created using collocated Reanalysis  $\Delta q/\Delta t$  values yields a map correlation coefficient of 0.92, with an NRMSD value of 5.0%. The MFC values were smoothed using a radius of 600 km for consistency with the resolution of the Lagrangian calculation. Mapped values using collocated NCEP  $\Delta q/\Delta t$  values were created by simply replacing the trajectory endpoint TES  $q$  values with those from the Reanalysis, recalculating the moisture budget, and mapping the results as in section 2.3.

[24] An exact agreement between the TES  $\Delta q/\Delta t$  and the NCEP MFC is not expected because of spatial and temporal sampling biases in the TES sample and known deficiencies in the NCEP humidity fields [e.g., Trenberth and Guillemot, 1995]; however, the comparison demonstrates the model's ability to represent the seasonal mean hydrologic cycle. The sampling biases are reduced by using the collocated values; differences here occur primarily through differences in vertical moisture profiles. The sensitivity of TES also varies vertically based on sky conditions, with peak sensitivity near 700 hPa in clear sky and near 450 hPa in regions with thick cloud [Lee *et al.*, 2011]. Fractional differences between TES and Reanalysis specific humidity values at 662.5 hPa over the ranges  $15^\circ\text{S} - 15^\circ\text{N}$ ,  $15^\circ\text{N/S} - 32.5^\circ\text{N/S}$ , and  $32.5^\circ\text{N/S} - 40^\circ\text{N/S}$  are 7.9% (TES more humid), 9.9%, and  $-2.2\%$ , respectively. TES water vapor validations with Cryogenic Frostpoint Hygrometers have shown TES measurements to be 5 – 10% higher below 700 hPa and 5 – 40% higher between 300 and 700 hPa [Shephard *et al.*, 2008].

However, Trenberth and Guillemot [1998] showed the NCEP-NCAR Reanalysis to be too dry in the tropics compared with NASA Water Vapor Project (NVAP) data. Nonetheless, Figure 4 and the map correlation coefficients provide confidence that the bulk seasonal features of the water cycles from  $40^\circ\text{S}$  to  $40^\circ\text{N}$  are captured in the simple trajectory budget model.

### 3.2. Changes in Isotopic Composition along Trajectories

[25] The average rate of change in mean  $\delta D$  (‰/day) for each set of trajectories is shown in Figure 5. One can immediately discern differences in the distribution from that of the  $\Delta q/\Delta t$  values (see Fig. 3), which is an indication of the unique information provided by the isotope ratio. R-squared values between  $\Delta q/\Delta t$  and  $\Delta \delta D/\Delta t$  for combined winter (JJA for  $0^\circ\text{S} - 40^\circ\text{S}$ , DJF for  $0^\circ\text{N} - 40^\circ\text{N}$ ) and summer hemispheres (opposite winter) are 0.36 and 0.47, respectively. This confirms that several different processes, and not simple Rayleigh theory, dictate the seasonal distribution of isotopic ratios and water vapor. The  $\delta D$  values generally decrease along the moisture pathways in the area in the Intertropical Convergence Zone, but they decrease predominantly near land regions known to experience a significant seasonal rainy season (i.e., for DJF, the Amazon Basin, northern Australia, and the Congo Basin; for JJA, Central America, Central Africa, and southeastern Asia). In these very humid regions, isotopic depletion by distillation along moisture pathways is



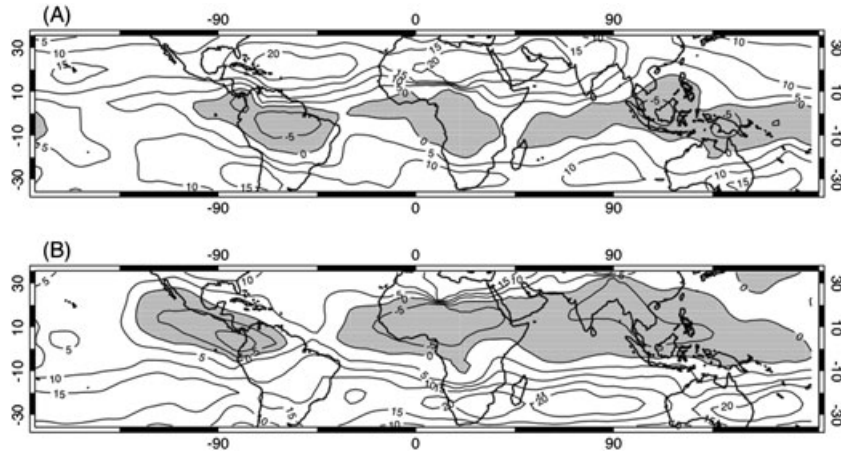


**Figure 5.** Average rate of change in  $\delta D$  values for the set of trajectories arriving at each grid point for DJF (A) and JJA (B). Line contour interval is 5‰/day. Shading indicates negative values.

an expected part of the regional hydrology [Brown *et al.*, 2008].

[26] Outside of these regions, and poleward of the tropics, the  $\delta D$  values increase on average along the trajectories. The increases are largest over the winter subtropical oceans, an area known for large surface evaporation rates [Trenberth and Guillemot, 1995]. In general, a steep vertical isotopic gradient in the background water vapor exists on long time scales because of the integrated history of condensation and follows the background thermal structure [Ehhalt *et al.*, 2005]. As such, these increases in the isotope ratio *en route* over the subtropics likely are linked to low-level mixing between isotopically heavy boundary layer air and very dry and isotopically depleted subsiding air parcels.

### 3.3. Source Specific Humidity and Isotopic Composition

[27] Source specific humidity ( $q_s$ ; Fig. 6) values can be interpreted on the basis of the numerical model to be the mean humidity of the air mass with which the parcels mix *en route* or, equivocally, the humidity to which the atmosphere would approach through mixing in the absence of sinks. Our calculations provide an estimate of the net source that is

integrated along all trajectories in the ensemble. Values of  $q_s$  can represent saturation specific humidity of a near-surface source (i.e., as in evaporation from the ocean) but also can describe the humidity of residual vapor following condensation (i.e., detrained from convection). Values of  $q_s$  will also include lateral mixing that is not resolved by the trajectory approach. High  $q_s$  values exist in climatologically moist and convectively active regions, which is consistent with an expectation that these locations provide a mechanism for vertical transport to the parcels over a 1–3 day time frame (e.g., the Amazon Basin, southern Africa, and Indonesia for DJF; and China, India, and the Caribbean Sea for JJA).

[28] The positions of extreme values and steepest spatial gradients of  $\delta D_s$  (Fig. 7) differ from those of  $q_s$ , again indicating the independence of information provided by the isotopologue measurements. For example, Amazonian DJF shows  $\delta D_s$  maxima farther south than  $q_s$  maxima. This offset in maxima may reflect moistening influences from transpired water, which generally emerges unfractionated from that found within soil water [Flanagan *et al.*, 1991] and is typically much less depleted than oceanic evaporation. Trenberth [1999] also found that local evapotranspiration influences atmospheric humidity more so in the southern Amazonian

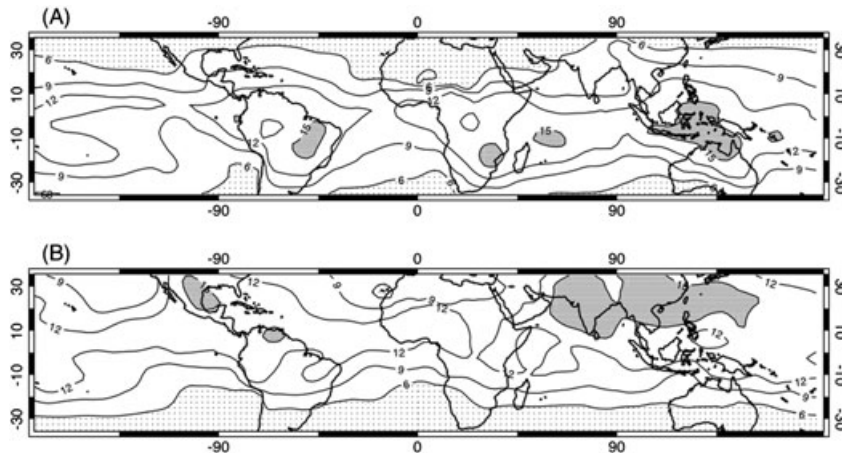


**Figure 6.** Average source specific humidity ( $q_s$ ) for the set of trajectories arriving at each grid point for DJF (A) and JJA (B). Line contour interval is 3 g/kg. Values greater than 15 g/kg are shaded, whereas those below 6 g/kg are stippled.

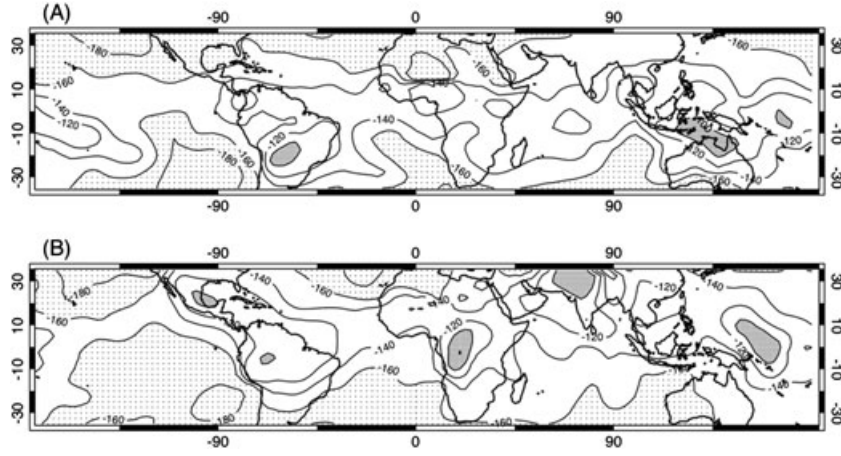


**Figure 7.** Mean isotopic composition of the source waters ( $\delta D_s$ ) for the set of trajectories arriving at each grid point for DJF (A) and JJA (B). Line contour interval is 20‰. Values greater than  $-100$ ‰ are shaded, whereas those below  $-160$ ‰ are stippled.

Basin during the wet season; however, the native resolution of the Lagrangian budget calculations used here ( $\sim 600$  km) prevents specific attribution. The  $\delta D_s$  values above  $-100$ ‰, which are consistent with those expected in marine boundary layer moisture [Craig and Gordon, 1965], are seen over convective and moist regions: the Amazon Basin, the Congo Region, the Pacific Warm Pool, the Yucatan, and southwest of the Gobi Desert during JJA; and over the southern Amazon and Indonesia during DJF. Outside of the tropics, and in particular over subtropical high-pressure zones,  $\delta D_s$  values are lower, indicating that the moisture available for turbulent transport to the parcels (i.e.,  $q_s$ ) has itself experienced substantial “rain out” during transport from some evaporative source region (e.g., the ocean). The lowest  $\delta D_s$  values ( $-180$ ‰ to  $-200$ ‰) coincide with areas known for seasonal subsidence (e.g., near the descending branch of the Walker Cell during both seasons, the Sahara region during DJF, and the oceanic region west of California). Although the positions of the regional isotopic signatures are interesting, analysis of the joint distributions of  $q_s$  and  $\delta D_s$  values is required to elucidate the formation processes that gave rise to the source waters available for turbulent exchange [Noone, 2012].

### 3.4. Local Mixing and Moistening Rates

[29] To understand the nature of the relationship between the isotope ratio and the processes underlying moistening, we consider the moistening rate. The mixing time scales ( $1/k$ ; Fig. 8) are the  $e$ -folding time scale for the mixing between the source and parcel moisture. Strong mixing (i.e., low  $1/k$  values) tends to occur over tropical land ( $1/k = 3.18$  days), to increase in strength during summer (2.68 days), and to have absolute maxima during tropical monsoons ( $< 2$  days; stippled area in Fig. 8) that typically are found to have strong convection. Although the least-depleted source moisture (high  $\delta D_s$ ) and the fastest mixing rates are both found within monsoonal regions, their precise positions differ within the regions (cf. Figs. 7 and 8). Within most monsoonal regions, the fastest mixing occurs with a more depleted source and is linked to strong local distillation and recycling effects (see below).

[30] Weaker mixing occurs over the subtropical oceanic region (4.31 days), with the weakest mixing ( $1/k > 5$  days; dark contouring in Fig. 8) found over areas of climatological subsidence (e.g., the Sahara Desert and near California during JJA, and the central Saharan Desert and near the west

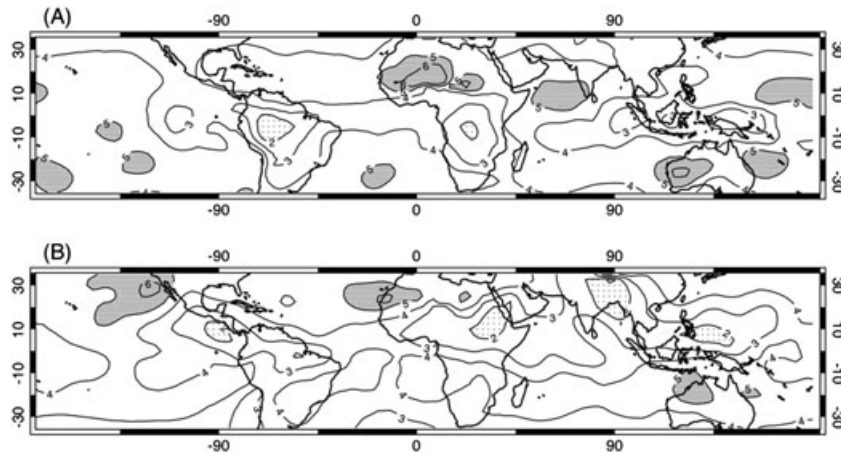


**Figure 8.** Mean mixing time scales ( $1/k$ ) for the set of trajectories arriving at each grid point for DJF (A) and JJA (B). Line contour interval is 1 day. Values greater than 5 days are shaded, whereas those below 2 days are stippled.



Australian coast during DJF). Excluding the central Sahara region, these slow mixing rates coincide with local upwelling zones and are consistent with the atmospheric stabilizing effects commonly attributed to low sea surface temperatures and stratiform cloud. These slow mixing rates, in conjunction with the low  $\delta D_s$  values discussed in section 3.3, confirm that exchange between the troposphere and the marine boundary is weak on average in these regions.

[31] Mixing time scales identify those regions where there is significant exchange between the source moisture and the parcels; however, a moistening efficiency,  $M$ , that describes the local fractional increase in parcel moisture can be defined as

$$M = \frac{G\Delta t}{\bar{q}}, \quad (7)$$

where  $\bar{q}$  is the average specific humidity value along the moisture transport pathways (i.e., the 500–825 hPa layer),  $G$  is the moistening rate (equation 2), and  $\Delta t$  is set to 1 day.

[32] Summertime  $M$  and  $1/k$  values are negatively correlated in the subtropics but positively correlated in the tropics (Fig. 9A). We have chosen to analyze correlations using the combined boreal and austral seasonal data (e.g., “summertime” subtropical data are DJF data from 15°S – 32.5°S combined with JJA data from 15°N – 32.5°N), because preliminary

seasonal analyses that discriminated between hemispheres yielded conclusions similar to those described here. Summertime  $M$  decreases as the large-scale vapor transport increases ( $r[M, q_{upstream}] = -0.72$ ) over the tropics, in agreement with past results over monsoonal regions [e.g., Trenberth, 1999]. This likely occurs because high ambient humidity buffers the effects of local mixing. The regression slope for the tropical summer data steepens from 1.8%/day for all data to 4.2%/day for just land points, and the positive correlation becomes stronger ( $r = 0.54$ ). Significant correlations between TES cloud top pressure measurements with  $1/k$  ( $r = 0.39$ ) and  $M$  ( $r = 0.51$ ) show that mixing rates increase and moistening efficiency decreases as convection deepens over summertime tropical land. Using isotopic information, we find that this decrease in  $M$  over tropical land with increased mixing rates is partially controlled by intense local moisture recycling, which leads to a drier and more depleted local moisture source than previously recognized.

[33] Moistening efficiency significantly increases as mixing strengthens during winter in the tropics and subtropics (Fig. 9B). Regression analysis reveals that  $M$  significantly decreases by 4.1%, 9.7%, and 2.4% for the tropics, subtropics, and midlatitudes, respectively, with 1 day increases in the mixing time scales. Thus,  $M$  is more than twice as sensitive to increases in mixing (e.g., shallow convection, turbulent exchange, or convective detrainment) in the wintertime subtropics than in other regions. Some caution should be used with this result, because the cost function results (Fig. 2) indicate that relative high variability in moisture pathways exists in the wintertime subtropics. However, calculated uncertainties on the mean model results are shown to be quite low for this region (see Appendix, Table A1). This mixing sensitivity result in the wintertime subtropics is important because this region represents a major source of water for the 500 – 825 hPa layer (Fig. 3), and the water vapor feedback here is sensitive to moisture perturbations resulting from the dry ambient air [Bony and Emanuel, 2005].

### 3.5. Source moisture mechanisms

[34] A variety of moistening processes can contribute to the regional source waters available for turbulent transport (i.e.,  $q_s$ ): mixing by shallow convection or turbulence, reversible adiabatic (cloud) processes, convective detrainment, and remoistening by the recycling of rainfall evaporation or postcondensational exchange. The moistening processes are best examined by comparing estimates of  $\delta D_s$  and  $q_s$  with predictions based on mixing and distillation [Noone, 2012]. Mixing lines in Figure 10 are initialized from a land source (i.e., transpiration) or from a source typical of marine boundary layer conditions. The transpiration mixing line, initialized from Global Network of Isotopes in Precipitation (IAEA/WMO, 2006)  $\delta D$  precipitation values in each region, assumes that rainfall is transpired unfractionated [Flanagan et al., 1991; Still et al., 2009] and then mixed with much drier air. This represents an upper limit to the  $\delta D$  value of water vapor influenced by transpired moisture and is much higher than the derived  $\delta D_s$  values. The marine mixing line also assumes direct mixing and is initialized with oceanic boundary layer air, assuming a relative humidity of 80% and SST of 27°C. This is a more reasonable upper bound and suggests that direct (dry) mixing of transpired water (i.e., unprocessed by

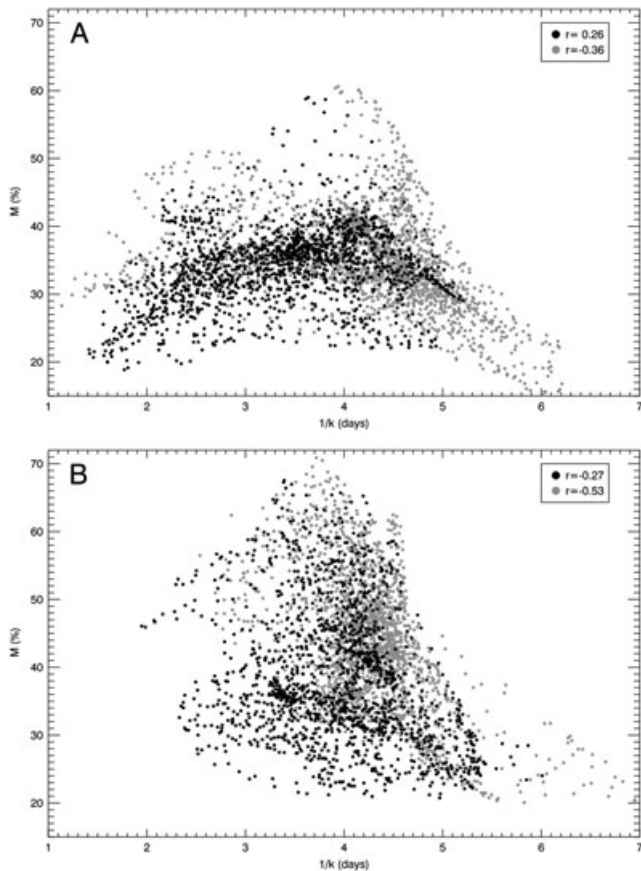


**Figure 9.** Scatterplots of moistening efficiency ( $M$ ) vs. mixing time scale ( $1/k$ ) values for the tropics (0° – 15°N/S, black) and subtropics (15° – 32.5°N/S, gray) during summer (A) and winter (B). Correlations in legend are statistically significant at the 99% confidence level.

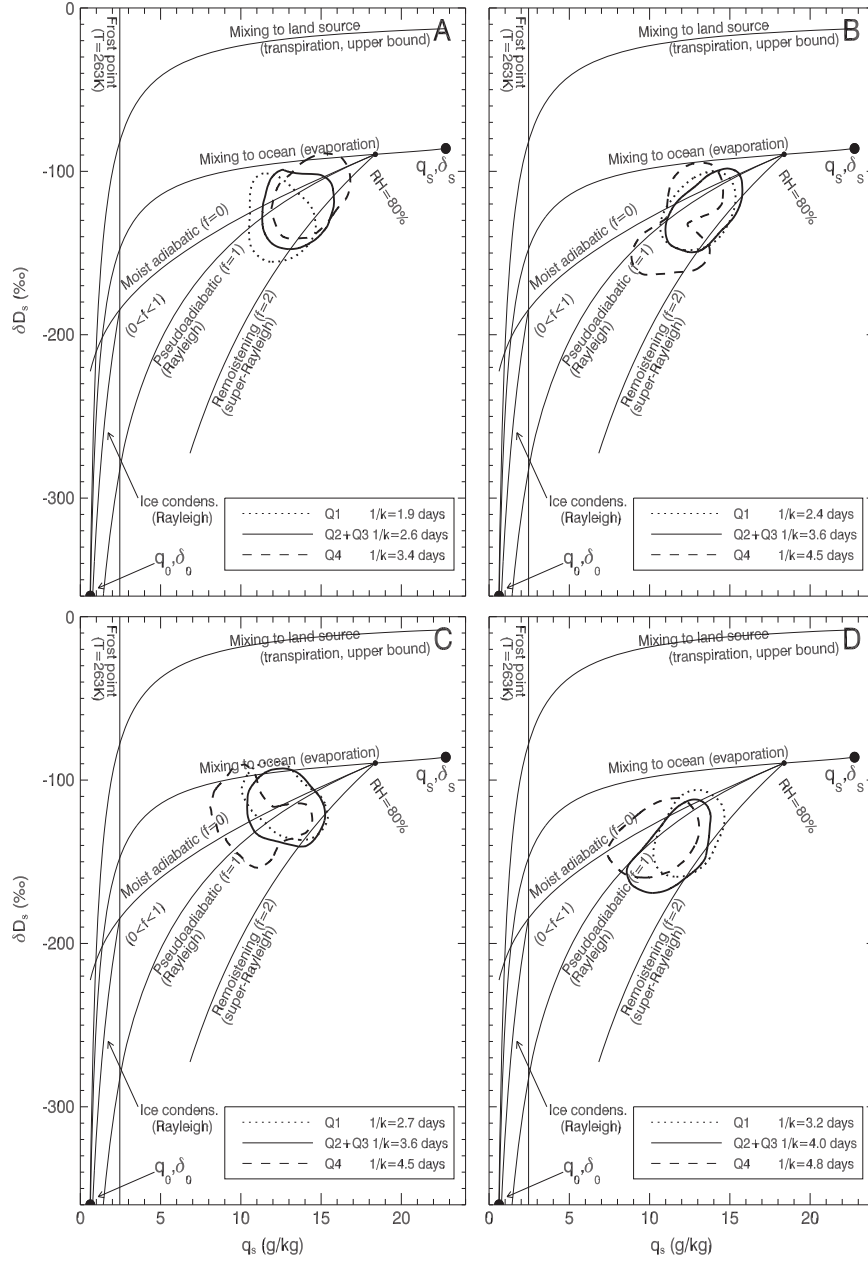


**Figure 10.**  $\delta D$  versus specific humidity for the source waters over tropical ( $0^\circ - 15^\circ N/S$ ) regions: summertime land (A) and ocean (B) and wintertime land (C) and ocean (D). Labeled lines indicate mixing and distillation processes (see Noone, 2012), assuming that the dominant global source of water is evaporation from the ocean ( $RH = 80\%$ ,  $SST = 27^\circ C$ ). Contours surround bins ( $1 \text{ g/kg}$  by  $10\%$ ) in which 2% or more of the data within each  $1/k$  partition (Q1, Q2 + Q3, and Q4) are found.

clouds) has limited influence on the humidity of air observed above the boundary layer even over land.

[35] The mean isotopic fractionation that occurs during condensation *en route* is recorded in the residual water vapor. Three condensation processes are represented (Fig. 10, labeled): moist adiabatic (condensed water is not removed from the system and thus continuously exchanges with the vapor [a reversible process and less fractionation]), Rayleigh distillation (condensed water is instantly removed from the system [nonreversible]), and “super-Rayleigh” distillation (additional fractionation beyond Rayleigh expectations) [Noone, 2012]. “Super-Rayleigh” distillation can represent

any intracloud or subcloud processes that lead to higher effective isotopic fractionation rates than those expected from vapor pressure differences of HDO and H<sub>2</sub>O [Rozanski *et al.*, 1993], including the effects of reintroduced residual vapor resulting from postcondensational exchange [Worden *et al.*, 2007; Risi *et al.*, 2008; Wright *et al.*, 2009b]. The positions of the data in Figure 10 suggest the processes that formed the local source water (i.e.,  $q_s$ ). The  $q_s$  data are partitioned into bins of mixing time scales ( $1/k$ ): Q1 is the quartile of data with the lowest 25% of regional mixing times (i.e., strongest mixing), Q4 is the quartile with the 25% highest, and Q2 + Q3 is the middle 50% of the distribution.

This partitioning thus separates regional formation processes associated with faster local mixing rates from those associated with slower local mixing rates and helps in discerning the different moistening characteristics within each region (e.g., over tropical land). Since uncertainties in the regional averages of the derived parameters (e.g.,  $q_s$  and  $1/k$ ) using our Monte Carlo approach are very small (Appendix A, Table A1), even small interregional and intraregional differences in parameter averages are useful for moisture budget comparisons.

[36] As noted in sections 3.3 and 3.4, regional average  $q_s$  and  $\delta D_s$  values are slightly higher, and mixing is stronger, over land ( $q_s = 14.6$  g/kg,  $\delta D_s = -133\text{‰}$ ,  $1/k = 3.1$  days) than ocean ( $13.9$  g/kg,  $-140\text{‰}$ ,  $3.8$  days) during tropical summer (cf. Figs. 6–8). Although these differences are consistent with the well-known increases in terrestrial humidity and convection characteristic of monsoons, the  $q_s$  and  $\delta D_s$  data positions in Figure 10A,B highlight the intraregional variations in moistening processes during the monsoon season that characterize the full nature of convection and moistening over tropical land and ocean. Although all the mixing rate partitions over tropical summertime land and ocean suggest limited direct (dry) mixing of boundary layer air into the local source moisture (i.e.,  $q_s$ ), the vast majority of data indicate that marine boundary layer air is processed by clouds before mixing into the local source moisture. The majority of data within all three contours in Figure 10A,B fall between the Rayleigh distillation line and the remoistening line, suggesting that moist convection associated with precipitating clouds and that moisture borne from postcondensational exchange both contribute substantially to the local source moisture and thus ultimately to tropical summertime moistening.

[37] Although clear similarities exist in the variety of moistening processes that occur over tropical summertime land and ocean, notable differences in these processes are exposed more clearly with the aid of correlation analysis. Over tropical land, the mixing rate partitions shown in Figure 10A indicate that  $q_s$  and  $\delta D_s$  both decrease as mixing rates increase. Significant correlations over tropical land confirm this effect [ $r(1/k, \delta D_s) = 0.42$ ,  $r(1/k, q_s) = 0.59$ ], which is a feature exclusive to tropical regions with very strong mixing (generally  $1/k < 3$  days; Fig. 11A) and is consistent with previous work that found anomalously depleted oceanic boundary layer moisture near organized convective storms [Lawrence *et al.*, 2004]. Model results in work by Risi *et al.* [2008] showed that, as convective mixing increases, the subcloud moisture pool is influenced more strongly by mixing with relatively dry and depleted storm downdrafts. This aspect of storm recycling is consistent with the decreased local moistening efficiency shown in Figure 9A during vigorous mixing in the tropical 500–825 hPa layer and here is associated primarily with strong terrestrial convection.

[38] The location of the probability distribution over tropical summertime ocean (Fig. 10B) is slightly different compared with that over the land surface. The lowest  $q_s$  values are associated with the slowest mixing (Q4), and the  $\delta D_s$  and  $q_s$  values do not decrease as mixing increases. Thus, the oceanic source waters, in general, do not become less moist and more isotopically depleted as mixing intensifies, as is the case over land.  $M$  is also consistent between partitions

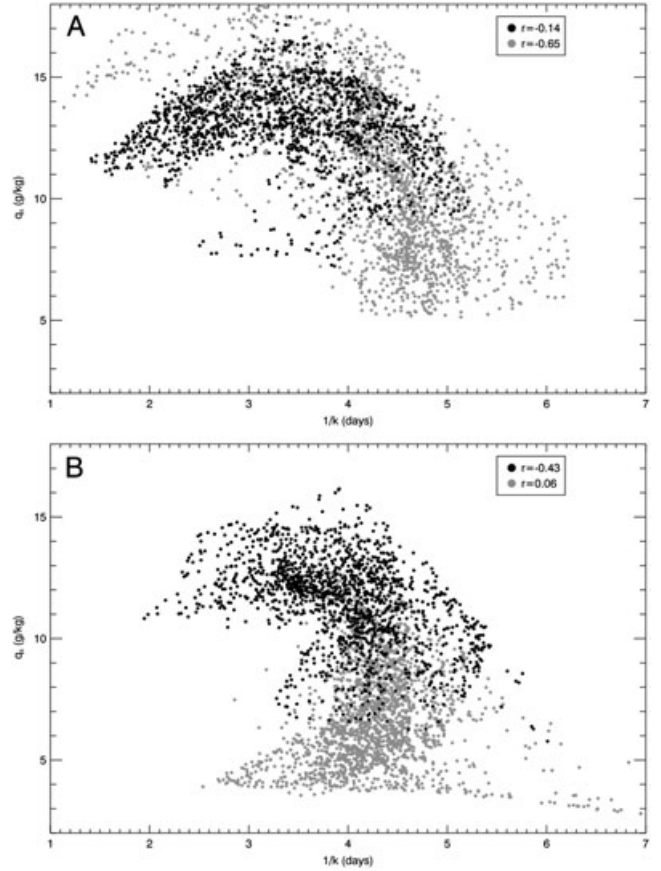


**Figure 11.** Scatterplots of source moisture ( $q_s$ ) vs. mixing time scale ( $1/k$ ) for the tropics ( $0^\circ - 15^\circ\text{N/S}$ , black) and subtropics ( $15^\circ - 32.5^\circ\text{N/S}$ , gray) during summer (A) and winter (B). Regional correlations in legend are statistically significant at the 99% confidence level.

(Q1 32%, Q4 34%) over ocean. The depleting and dehydrating effect on the source waters (and hence  $M$  values) during tropical summertime is found to occur only during intense mixing (cf. Figs. 9A and 11A). The weak positive correlation between all tropical summertime mixing time scale and moistening efficiency values (Fig. 9A) becomes insignificant using paired data with  $1/k$  values greater than 2.3 days and in fact significantly negative using data with  $1/k$  values greater than 2.8 days (see shape in Fig. 9A). Paired data (using both land and ocean points) below  $1/k = 2.3$  days show a strong positive correlation of 0.56 and a 13.6% increase in  $M$  per day increase in  $1/k$ . Thus, it is only under very strong mixing conditions that source vapor is drier and more depleted and therefore is ultimately less efficient in locally hydrating the 500–825 hPa layer. This result, which was found with a simple model in conjunction with moisture and HDO/H<sub>2</sub>O observations, is consistent with simplified oceanic model simulations [Risi *et al.*, 2008] showing that strong convective recycling can act to dehydrate and deplete the boundary layer water vapor pool. However, because the simulations by Risi *et al.* [2008] were over ocean, it remains unclear whether the balance of mechanisms would remain the same over tropical land.

[39] The locations of the tropical wintertime data suggest that reversible moist processes are more prevalent over land



(Fig. 10C) than ocean (Fig. 10D). Calculations indicate that  $>50\%$  of the local gross moistening ( $G$ ) over land, and  $\sim 10\%$  of  $G$  over ocean, is associated with reversible moist adiabatic processes, with the remainder of  $G$  in each case linked to moist convection occurring within/near precipitating clouds. These percentages of total land or ocean  $G$  values are estimated by calculating the  $G$  values associated with those grid points that are most close to the reversible moist adiabatic lines in Figure 10C,D and comparing them with the total  $G$  found using all tropical wintertime land or ocean grid points. The more frequent occurrence of moist convection over wintertime ocean than over land is likely caused by ocean conditions during the winter monsoon, in which the high heat capacity of ocean waters allows residual heat to drive more moist convection over ocean than over cooler land nearby. In contrast to terrestrial storms during the summer monsoon,

the winter monsoon shows that oceanic storms with high isotopic “rainout” and strong mixing are the most efficient at moistening the 500–825 hPa layer [ $r(M, 1/k) = -0.30$ ,  $r(M, \delta D_s) = -0.59$ ,  $>99\%$  confidence]. However, as during summer, this effect is also related to large-scale moisture advection, since  $M$  tends to decrease as the upstream parcel humidity ( $q_{upstream}$ ) increases.

[40] In the subtropics, local source moisture formation processes are separated clearly by mixing rates during summer and are separated less clearly during winter (Fig. 12A–D). The locations of the probability distributions in Figure 12A,B suggest that moisture processed by postcondensational exchange is associated with strong mixing (Q1) during summer, and this moisture within the Q1 bins is estimated to account for  $\sim 36\%$  of  $G$  over both land and ocean. These data are from near the Asian and North American monsoon regions

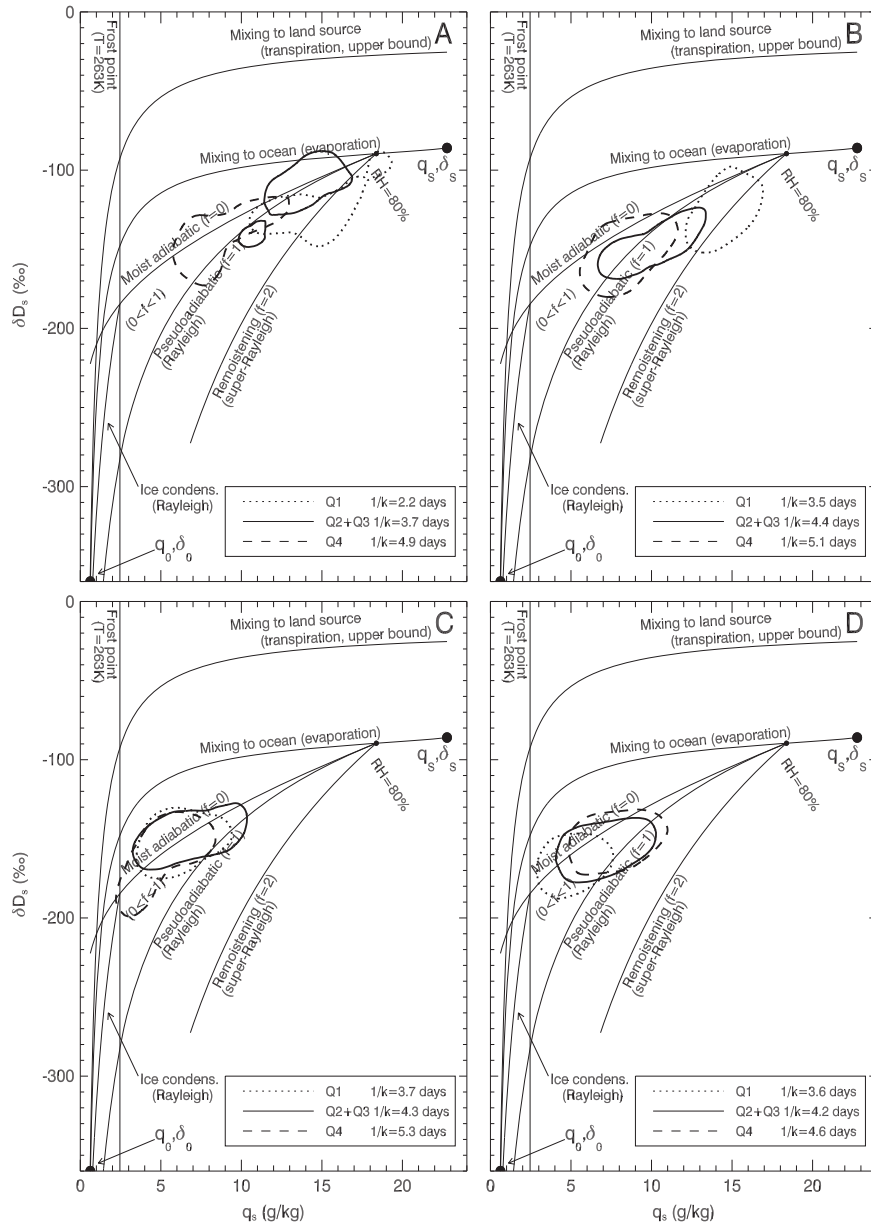


**Figure 12.** As in Figure 10, but for the subtropical (15°–32.5°N/S) regions.

(not shown), where strong seasonal convection has been linked to postcondensational exchange using a GCM [Field *et al.*, 2010]. The location of the Q2 + Q3 data in Figure 12A suggests that a substantial portion of the source moisture over land during summer is slightly fractionated marine boundary layer moisture (i.e., shallow convection), yet the expected isotopic signature of shallow convection is largely absent over ocean (Fig. 12B). These results are broadly consistent with those of Couhert *et al.* [2010], who found that dynamic transport by convection was most influential on tropospheric humidity over land during summer. The results here also suggest that the moistening effects of condensate evaporation are most influential near subtropical monsoonal regions. The moistening in the subtropics during winter is characteristically different from that during summer, for which the data suggest that moisture is processed mainly through nonprecipitating clouds, in agreement with past work [Lee *et al.*, 2011]. Even with relatively depleted and dry source moisture compared with other regions, the local moistening efficiency ( $M$ ) values in this region during winter are high (42% over land, 45% over ocean) since the overlying atmosphere is extremely dry.

[41] Because the TES measurements are sensitive to clouds, care must be taken to ensure that results are robust in spite of a possible sampling bias. The results were checked to confirm that the findings are not an artifact of cloud-related biases in the data by repeating the analysis with only clear-sky data. Although some differences exist in the number and distribution of the clear-sky- vs. all-sky-derived parameters over some geographical regions, the primary conclusions are robust. This likely results from analyzing the spatial distributions of the derived parameters (e.g.,  $\delta D_s$  and  $q_s$ ) in small regions (e.g., tropical land only) and during specific seasons (i.e., DJF or JJA) in which residual vapor detrained from local clouds is most likely to influence the nearby clear air. For example, prior work [Lee *et al.*, 2011] showed that air parcels in regions of precipitating clouds are often more depleted in HDO and more moist than parcels in regions of clear sky or in regions of nonprecipitating clouds, indicating an additional fractionation process, such as rainfall evaporation, or isotope

exchange between raindrops and the surrounding air during convective activities. The comparison using clear-sky and all-sky data in tropical terrestrial convective regions did show notable differences in the quantity of data available (i.e., these are cloudy regions), yet the overall spatial distribution of the  $\delta D_s$  and  $q_s$  clear-sky data led to conclusions almost identical to those we draw below from the all-sky data. This underscores that moisture processes that occur within clouds are recorded by HDO/H<sub>2</sub>O values in the adjacent and residual clear-sky air.

### 3.6. Dehydration Mechanisms

[42] The difference between net isotopic fractionation ( $\alpha$ ; found from the mass budget model) and equilibrium fractionation ( $\alpha_e$ ) gives a measure of different types of cloud processes (i.e., nonprecipitating clouds) and postcondensational exchange. The equilibrium fractionation factor ( $\alpha_e$ ) is based on the temperature of condensation and is estimated here by using the average dew-point temperature in each individual trajectory. Effective fractionation that is greater than the equilibrium value ( $\alpha - \alpha_e > 0$ ; dark shading in Fig. 13) occurs primarily over terrestrial monsoonal regions and the Pacific Warm Pool, which is in agreement with the spatial distribution of excess depletion in residual vapor (i.e., beyond Rayleigh expectations) found from past analyses of TES observations [Brown *et al.*, 2008] and of comprehensive models [e.g., Wright *et al.*, 2009b; Field *et al.*, 2010]. Noone [2012] showed that enhanced fractionation can be a signature of exchange between falling rain and a relatively dry environment. We find here that enhanced fractionation occurs primarily over regions with high ambient humidity, so quantification of postcondensational exchange below the cloud base would require information on the drop size spectrum and isotopic composition of the subcloud air [Bolin, 1958].

[43] During the summer in both hemispheres (at latitudes less than 40°N or S),  $\alpha - \alpha_e$  significantly increases with increased mixing ( $r[\alpha - \alpha_e, I/k] = -0.37$ ) and significantly decreases with increasing local moistening efficiency ( $r[\alpha - \alpha_e, M] = -0.42$ ).

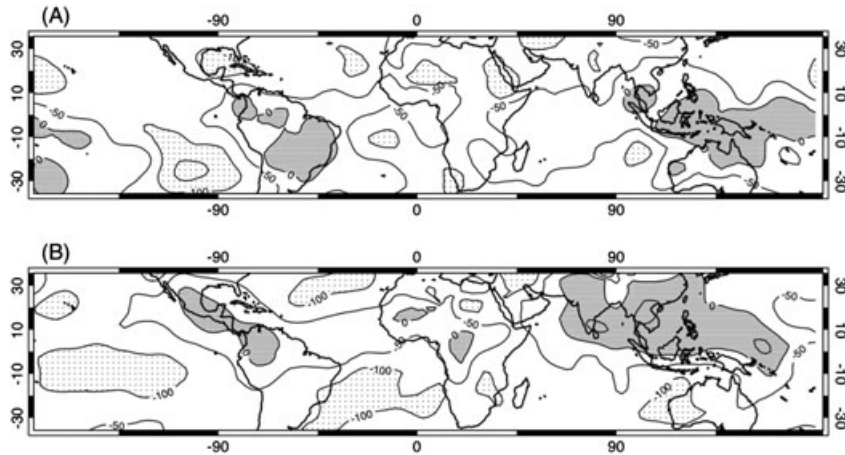


**Figure 13.** Difference between effective and equilibrium fractionation factors,  $(\alpha - \alpha_e, \%)$  for (A)DJF (A) and (B)JJA (B). Shading indicates regions where  $\alpha - \alpha_e$  is greater than zero, whereas stippling indicates regions where  $\alpha - \alpha_e$  is less than  $-100\%$ . Contour interval is  $50\%$ .

Considering just the summertime tropics, similar correlations ( $r[\alpha - \alpha_e, I/k] = -0.34$  and  $r[\alpha - \alpha_e, M] = -0.59$ ) illustrate that anomalous depletion reaches its maximum when moistening efficiency is low in these highly convective regions. This suggests that reduced localized moistening and strong convective mixing are requirements for super-Rayleigh isotopic depletion of water vapor. This aligns with our results described in sections 3.4 and 3.5 and provides additional observational support for the processes proposed by *Risi et al.* [2008] to explain strong isotopic depletion during convection, which required a substantial connection (recycling) between unsaturated downdrafts and the subcloud layer to produce a drier and more depleted vapor source for subsequent precipitation.

[44] Reversible moist processes, in which condensate is not removed from the system but instead remains in isotopic equilibrium with the vapor, reduce the fractionation rates estimated in the Lagrangian model. The above correlation analysis revealed that  $\alpha - \alpha_e$  is lowest in regions with weak mixing but high local moistening efficiency. *Noone* [2012] showed that differences in effective and equilibrium fractionation (i.e.,  $\alpha$  and  $\alpha_e$ ) can provide a rough approximation of liquid precipitation efficiency (precipitation rate divided by condensation rate). This can be tested empirically using correlation analysis of  $\alpha - \alpha_e$  vs. the ratio of precipitation and moisture loss rates.

[45] With the precipitation radar on the Tropical Rainfall Monitoring Mission satellite monthly mean precipitation data (version 3B43, [Huffman et al., 1995]), a mass-weighted precipitation rate ( $P_{TRMM}$ ) is found using the levels in the TES retrieval (500–825 hPa). Given the general definition from *Noone* [2012], a liquid precipitation efficiency is then calculated simply as  $P_{TRMM}/L$ , where  $L$  is the modeled moisture loss rate (i.e., the condensation rate, expressed in millimeters per day for the 500–825 hPa layer). The relationships between  $\alpha - \alpha_e$  and  $P_{TRMM}/L$  are shown in Figure 14, in which correlation coefficients for  $\alpha - \alpha_e$  and  $P_{TRMM}/L$  are  $r=0.68$  (tropics only) and  $r=0.58$  (subtropics only). These correlations are similar to the respective correlations between  $\alpha - \alpha_e$  and  $L$  (0.67 and 0.61) and weaker than the correlations between  $\alpha - \alpha_e$  and  $P_{TRMM}$  (0.78 and 0.73). In the same geographical regions but with wintertime data,  $r(\alpha - \alpha_e, P_{TRMM}/L) = 0.60$  and 0.17,  $r(\alpha - \alpha_e, L) = 0.46$  and 0.30, and  $r(\alpha - \alpha_e, P_{TRMM}) = 0.70$  and 0.27. Thus, except for the subtropical regions during winter, the relationships between differences in effective and equilibrium fractionation rates with precipitation efficiency are fairly strong, yet  $\alpha - \alpha_e$  is more strongly correlated with the regional precipitation rates. We note that all  $\alpha - \alpha_e$  values are less than zero in the subtropical regions during winter, which is consistent with the results described in the previous section showing that moist processes in this region are largely associated with

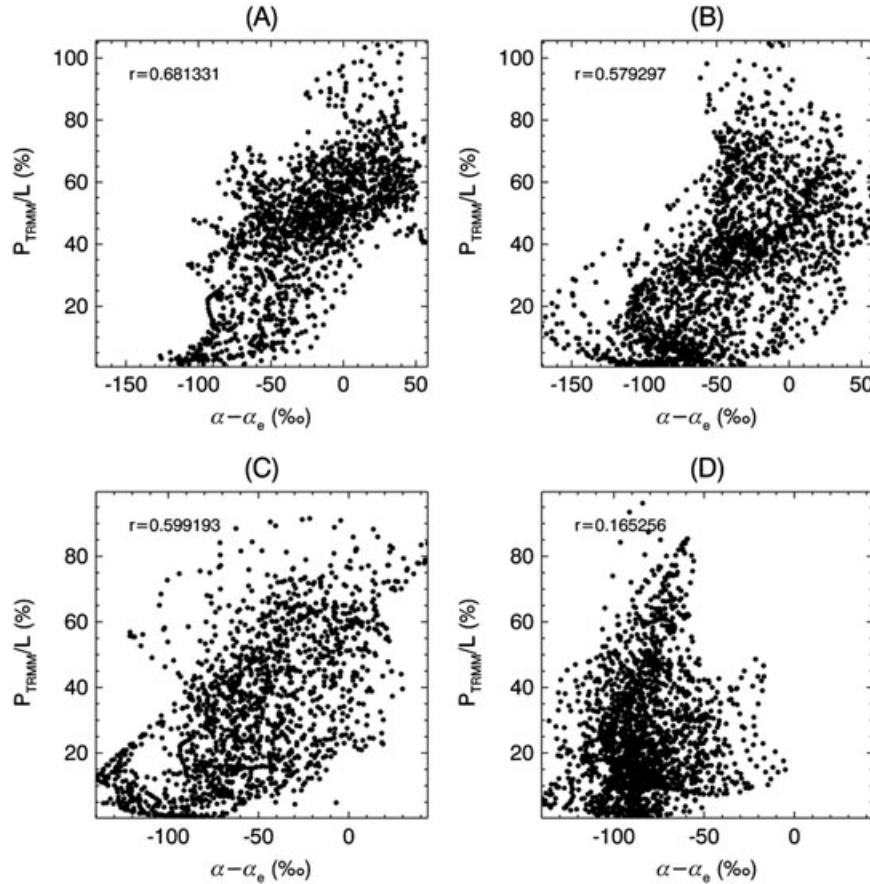


**Figure 14.** Scatterplots of  $P_{TRMM}/L$  (%) and  $\alpha - \alpha_e$  (‰) for tropical summertime (A) and wintertime (C) and subtropical summertime (B) and wintertime (D).



reversible adiabatic exchange (i.e., moisture exchanges occur through nonprecipitating clouds).

#### 4. Conclusions

[46] Characteristics of processes that moisten the 500 – 825 hPa layer of the troposphere were identified by using the isotopic composition and humidity of air parcels. This Lagrangian-type analysis was found to be more sensitive to perturbations in moisture source and source isotopic composition than to mixing rates, loss rates, or isotopic fractionation. Additionally, the model sensitivity is maximized in tropical terrestrial regions, and these regions are thus the most well-constrained region for this model. The model is simple by design, so care must be taken to limit analyses of results to those features that are robust to the model's level of complexity. The three key advantages of the model used here are 1) that the mass balance is constrained by isotopic observations, 2) that the air mass transport pathway is accounted for, and 3) that moistening and condensation are both allowed. By interpreting both the physical significance of the isotopic state of the moisture source vapor and the efficiency of the bulk isotopic fractionation that occurs in cloudy regions, unique information regarding atmospheric moistening and dehydration emerges from our isotopic model.

[47] The analysis identified the different source water that mixes into passing air parcels, the formation processes that led to these moisture sources, the time scales over which this mixing occurs, and the resultant fractional increases in large-scale humidity values associated with local moisture sources. Local moisture sources were found 1) to have nonnegligible hydrating effects over a 1 – 3 day time frame on arriving air parcels; 2) to be associated primarily with vapor detrained from precipitating cloud systems in the moist tropical regions, with vapor resulting from postcondensational exchange and reversible processes in the summertime subtropics and with vapor associated with reversible processes over dry tropical land and over the wintertime subtropics; and 3) to have the largest impact on fractional moisture gains (i.e., moistening efficiency) in the wintertime subtropical regions (15° – 25°N/S). Strong large-scale moisture transport is confirmed to limit the effects of local sources on tropical moistening efficiency [Trenberth, 1999]. However, the analysis revealed that, during terrestrial monsoons, the isotopic composition of the source moisture becomes more depleted as mixing rates increase. In these areas of heavy rainfall, strong isotopic fractionation and dehydration during intense convective storms suggest that the local moisture source for convective storms becomes drier and more depleted as a result of moisture recycling, which subsequently limits local moistening efficiency yet increases bulk isotopic fractionation by clouds during very vigorous convection. This mechanism is similar to the modeled by Risi *et al.* [2008], in which highly depleted moisture within unsaturated downdrafts was found to be re-entrained into convective storms, leading to anomalous depletion of subsequent rainfall (i.e., to contribute to an “amount effect”) that forms from the increasingly depleted moisture source. Evidence for this mechanism in TES data was recently found near convective clouds in the western Pacific Ocean [Lee *et al.*, 2011]. Over land, evidence was found here for dehydration of boundary layer air by strong

convection that was previously predicted in a simplified model [Risi *et al.*, 2008]. This mechanism may contribute to the amount effect observed in historical climate signals derived from isotope ratios in tropical ice cores [Wushiki, 1977; Grootes *et al.*, 1989]. However, lack of knowledge of the vertical isotopic profiles of water vapor and raindrop size spectra in these regions precludes proper quantification of the effects of isotopic depletion in the vapor pool from postcondensational exchange and subsequent recycling of vapor. This study paves the way for future work to use both water vapor and precipitation isotopic data to elucidate the atmospheric dynamics, cloud microphysics, and isotopic exchanges that must occur to produce very depleted rainfall (i.e., the amount effect) in monsoonal regions.

[48] Results show that postcondensational exchange is an important component to local moistening over the summertime subtropics (~36% of regional average  $G$  is attributed to this process), which tends to raise the total local fraction of water in the 500 – 825 hPa layer by approximately 5% per day. For a qualitative comparison between our Lagrangian model results and those found with a much more coarse global model, consider the ~20% rainfall evaporation fraction needed by Worden *et al.* [2007] to achieve balance in their moisture and isotope budgets in the subtropics. Their study assumed a condensation rate of 8 mm/day (~2.7 [g/kg]/day for the 500 – 825 hPa layer). When assuming hydrologic balance (i.e.,  $G - L = 0$ ), ~20% of this condensation is returned as vapor through rainfall evaporation and therefore represents a  $G$  value of 0.55 (g/kg)/day. This is approximately 35% of total subtropical  $G$  (1.56 [g/kg]/day) derived from our model over the subtropics (see Table A1), and this percentage is generally consistent with our ~36% value for local moistening in the summertime subtropics via rainfall evaporation and/or postcondensational exchange. This postcondensational exchange process is also active during tropical summer but has limited effects on the large-scale humidity. That postcondensational exchange is important for atmospheric hydrology and is identifiable by using isotopic methods agrees with other work [e.g., Worden *et al.*, 2007; Brown *et al.*, 2008; Wright *et al.*, 2009b; Field *et al.*, 2010]. There remains a clear need, however, to decipher further the different characteristics of postcondensational exchange, and their effects on lower tropospheric humidity, in dry vs. moist regions using observational data sets that include isotopic information. Better understanding of remoistening by evaporation of condensate will be useful for improving parameterizations in current climate models, which currently produce drier lower-tropospheric air than is observed during convective storms [Mapes *et al.*, 2009].

[49] Although the tropical regions were shown to have active convection, strong mixing, and large gross moistening values, the local effects on the large-scale humidity were shown to be minimal. In contrast, vapor associated with reversible processes (i.e., cloud “burn off”) dominates local moistening in the dry subtropics, and the resultant local gross moistening, though modest in magnitude compared to that in the tropics, contributes significantly to the (low) large-scale humidity. Fractional increases in water vapor abundance (as in  $M$ ) in this region substantially impact the global water vapor feedback [Pierrehumbert, 1999], so local moistening from cloud evaporation over the wintertime subtropics is important to the global energy balance.

[50] Finally, the differences between mean effective and equilibrium fractionation rates (i.e.,  $\alpha - \alpha_e$ ) were shown to correlate with precipitation efficiency and convective recycling. Although the results have limitations linked to the simplicity of the physics included in the model and data sampling (including the use of monthly mean TRMM precipitation instead of collocated precipitation data), the spatial relationships found provide confidence that more advanced models can utilize isotopic fractionation to quantify precipitation efficiency effectively. More information about the vertical profiles of  $\delta D$  is required to resolve this relationship more clearly, because this information is needed to resolve subcloud isotopic exchange in humid regions. Recently, TES HDO/H<sub>2</sub>O data with more degrees of freedom (i.e., approximately two vertical data points per nadir measurement can be obtained) has been released [Worden *et al.*, 2012]. In addition, boundary layer HDO/H<sub>2</sub>O ratios are currently measured via satellite by the SCIAMACHY instrument [Frankenberg *et al.*, 2009], and stratospheric HDO/H<sub>2</sub>O ratios are measured with the MIPAS instrument [Steinwagner *et al.*, 2007; Losow *et al.*, 2011], although the uncertainties associated with both data sets are notable. These increases in information may make it possible to distinguish regions where both postcondensational exchange and reversible processes operate simultaneously (which tends to obscure the relationships between  $\alpha - \alpha_e$  and  $P_{TRMM}/L$ ) and will be further explored in a subsequent study. Further distinction of the relevant moist processes can be facilitated by undertaking an analysis that merges the isotopic constraints with more sophisticated dynamic models.

[51] **Acknowledgments.** Support for this study came from a Graduate Research Environmental Fellowship from the U.S. Department of Energy's Office of Biological and Environmental Research, funding from the Jet Propulsion Laboratory, and grants from the NASA Atmospheric Composition Program (NNX08AR23G) and the NASA Energy and Water Cycle Study (07-NEWS07-0020). A portion of the research described in this paper was carried out at the Jet Propulsion Laboratory, California Institute of Technology, under a contract with the National Aeronautics and Space Administration. The NASA ROSES Aura Science Team NNN07ZDA001N-AST 07-AST07-0069 contributed to the support of the analysis.

## Appendix Climatological Statistics

[52] Many observations are used to construct mean conditions. The Lagrangian model parameters that are obtained though minimizing the cost function,  $J$  (equation 5), must similarly be those relevant for mean estimates. The mean quantities are

$$\overline{G_q} = \overline{k(q_s - q)} \quad (A1)$$

and

$$\overline{L_q} = \overline{aq} \quad (A2)$$

where the overbar is the traditional arithmetic ensemble mean, and  $G_q$  and  $L_q$  need not be equal at the regional scale (i.e.,  $G_q - L_q$  is the net moisture divergence for the atmospheric region of interest, taken in this study as the 825 – 500 hPa layer observed via TES). An averaging scheme is used to ensure that the appropriate parameters arise:

$$\overline{L_q} = \overline{aq} = \left( \frac{\overline{aq}}{\tilde{q}} \right) \tilde{q} = \tilde{a} \tilde{q} \quad (A3)$$

where the tilde denotes the mass weighted mean defined by the term in parentheses. In general,  $\tilde{a} \neq \bar{a}$ . Similarly, for the mean gain of water into the parcels en route,

$$\overline{G_q} = \overline{k(q_s - q)} = \tilde{k}(\tilde{q}_s - \tilde{q}). \quad (A4)$$

[53] For the HDO budget, a similar ensemble averaging is adopted:

$$\overline{L_x} = \overline{\alpha ax} = \left( \frac{\overline{\alpha ax}}{\tilde{q}} \right) \tilde{x} = \hat{\alpha} \left( \frac{\overline{aq}}{\tilde{q}} \right) \tilde{x} = \hat{\alpha} \tilde{a} \tilde{x}, \quad (A5)$$

with  $\hat{\alpha}$  an appropriate effective (mean) fractionation, which is strictly a loss-rate-weighted mean rather than the usual mass-weighted mean and can be determined as

$$\hat{\alpha} = \frac{\overline{\alpha a q}}{\overline{a q}}, \quad (A6)$$

and, similarly for the gain of HDO into the parcels en route, the averaged equation is

$$\overline{G_x} = \overline{k\mu(x_s - x)} = \tilde{k}\mu(\tilde{x}_s - \tilde{x}). \quad (A7)$$

[54] Thus, the challenge is to determine the climatological mean values of the model parameters ( $\tilde{a}, \tilde{k}, \tilde{q}_s, \tilde{x}_s$ , and  $\hat{\alpha}$ ) that best match the ensemble of observations making up the climatological mean specific humidity ( $\overline{q_{obs}}$ ) and isotopic ratio ( $R_{obs}$ ) at the trajectory end points. Once determined from minimization of the cost function, the estimated parameters ( $\tilde{a}, \tilde{k}, \tilde{q}_s, \tilde{x}_s$ , and  $\hat{\alpha}$ ) are used in calculation of seasonal mean values of  $\overline{G_q}, \overline{G_x}, \overline{L_q}$ , and  $\overline{L_x}$  and the isotopic ratio of water entering ( $R_G$ ) and leaving ( $R_L$ ) the atmospheric region of interest.

## Mean and Error Estimates by Ensemble Method

[55] Uncertainties with regard to the estimated parameters are determined via a Monte Carlo method based on the known error estimates for  $q$  and  $R$  found from the TES retrievals. A 500-member Monte Carlo ensemble is created by perturbing the TES  $q$  and  $R$  values at both the upstream and the arrival sites (i.e., the trajectory endpoints) by an amount proportional to the TES retrieval uncertainty scaled by normally distributed random numbers with  $\pm 1$  standard deviation. This approach is consistent with the TES Gaussian error model. The trajectory budget model is optimized for each member of the ensemble, with the ensemble mean reported as the optimal value. The errors for each parameter are calculated as  $\bar{\sigma} = \sigma/\sqrt{n}$ , where  $n$  is the number of ensemble members, and  $\sigma$  is the standard deviation among the 500 ensemble members.

[56] In Table A1, the land regions show a greater error (roughly twice as large) for the means than the oceanic regions. This is due largely to fewer observations over land, which is a result of lower-quality retrievals over land because of multilayer clouds and surface emissivity anomalies [Worden *et al.*, 2004]. However, the fractional error of the mean of all parameters is less than 1%. The uncertainty for

the calculated  $\delta D$  values of the moisture gains and losses ( $\delta D_G$  and  $\delta D_L$ ) are largest, at roughly 2 – 6‰.

**Table 1A.** Mean and Error of the Mean for Various Parameters Derived from Optimization of the Mass Balance Model with TES Observations<sup>a</sup>

Parameter	Units	Land Mean	Land Error	Ocean Mean	Ocean Error
Tropical Regions (0° to 15°)					
$q_s$	g/kg	12.8	0.16	12.1	0.07
$\delta D_s$	‰	–124	2.01	–137	1.01
$1/k$	days	3.17	0.05	3.79	0.03
$1/a$	days	3.21	0.08	3.10	0.03
$\alpha$	unitless	1.080	0.006	1.069	0.002
$G$	(g/kg)/day	2.17	0.04	1.87	0.02
$L$	(g/kg)/day	2.27	0.04	1.97	0.02
$G-L$	(g/kg)/day	–0.09	0.01	–0.10	<0.01
$\delta D_G$	‰	–97	5.63	–112	2.24
$\delta D_L$	‰	–83	4.77	–106	2.03
Subtropical Regions (15° to 32.5°)					
$q_s$	g/kg	9.49	0.07	8.85	0.03
$\delta D_s$	‰	–142	1.15	–154	0.57
$1/k$	days	4.06	0.03	4.31	0.01
$1/a$	days	3.45	0.06	3.24	0.02
$\alpha$	unitless	1.066	0.003	1.053	0.001
$G$	(g/kg)/day	1.56	0.02	1.31	0.01
$L$	(g/kg)/day	1.62	0.02	1.22	0.01
$G-L$	(g/kg)/day	–0.06	<0.01	0.09	<0.01
$\delta D_G$	‰	–121	2.97	–138	1.05
$\delta D_L$	‰	–114	2.72	–133	1.19
Midlatitude Regions (32.5° to 40°)					
$q_s$	g/kg	7.88	0.03	5.50	0.01
$\delta D_s$	‰	–157	0.82	–169	0.49
$1/k$	days	3.95	0.02	3.82	0.01
$1/a$	days	2.98	0.03	2.90	0.01
$\alpha$	unitless	1.059	0.002	1.062	0.001
$G$	(g/kg)/day	1.26	0.01	0.83	<0.01
$L$	(g/kg)/day	1.26	0.01	0.89	<0.01
$G-L$	(g/kg)/day	0.01	<0.01	–0.06	<0.01
$\delta D_G$	‰	–137	2.44	–150	1.07
$\delta D_L$	‰	–133	1.64	–140	0.94

<sup>a</sup>Statistics are derived from a Monte Carlo ensemble. Values combine results from DJF and JJA averages.

[57] Beyond uncertainty, other potential sources of error are associated with the spatial and temporal distribution of the seasonal trajectories and the fact that TES measurements are biased toward mostly clear-sky conditions. Although TES measures mostly clear-sky conditions, the dominant seasonal moistening processes that occur for each region are recorded in the isotopic distribution in the (residual) vapor nonetheless. For instance, it would be expected that clear-sky, residual moisture immediately following a large storm would remain relatively depleted in HDO (e.g., from isotopic “rain out”) compared with the seasonal mean isotopic composition.

## References

Angert, A., J. E. Lee, and D. Yakir (2008), Seasonal variations in the isotopic composition of near-surface water vapour in the eastern Mediterranean, *Tellus Ser. B*, 60(4), doi:10.3402/tellusb.v60i4.16953.  
 Araguas-Araguas, L., K. Froehlich, and K. Rozanski (1998), Stable isotope composition of precipitation over southeast Asia, *J. Geophys. Res.*, 103(D22), 28, 721–728, 742, doi:10.1029/98JD02582.  
 Betts, A. K. (1990), Greenhouse warming and the tropical water-budget, *Bull. Am. Meteorol. Soc.*, 71(10), 1464–1465.

Bolin, B. (1958), On the use of tritium as a tracer for water in nature, paper presented at Proceedings of 2nd International Conference on Peaceful Use of Atomic Energy, p. 336–343.  
 Bony, S., and K. A. Emanuel (2005), On the role of moist processes in tropical intraseasonal variability: Cloud-radiation and moisture-convective feedbacks, *J. Atmos. Sci.*, 62(8), 2770–2789.  
 Bony, S., C. Risi, and F. Vimeux (2008), Influence of convective processes on the isotopic composition ( $\delta$  O-18 and  $\delta$  D) of precipitation and water vapor in the tropics: 1. Radiative-convective equilibrium and Tropical Ocean-Global Atmosphere-Coupled Ocean-Atmosphere Response Experiment (TOGA-COARE) simulations, *J. Geophys. Res.*, 113(D19).  
 Brent, R. P. (1972), Algorithms for minimization without derivatives, *xii*, 195 p., Prentice-Hall, Englewood Cliffs, N.J.  
 Brown, D., J. Worden, and D. Noone (2008), Comparison of atmospheric hydrology over convective continental regions using water vapor isotope measurements from space, *J. Geophys. Res.*, 113(15).  
 Cappa, C. D., M. B. Hendricks, D. J. DePaolo, and R. C. Cohen (2003), Isotopic fractionation of water during evaporation, *J. Geophys. Res.*, 108(D16), doi:10.1029/2003jd003597.  
 Clough, S. A., M. W. Shephard, J. Worden, P. D. Brown, H. M. Worden, M. Luo, C. D. Rodgers, C. P. Rinsland, A. Goldman, L. Brown, S. S. Kulawik, A. Eldering, M. Lampel, G. Osterman, R. Beer, K. Bowman, K. E. Cady-Pereira, and E. J. Mlawer (2006), Forward model and Jacobians for Tropospheric Emission Spectrometer retrievals, *IEEE Trans. Geosci. Remote Sens.*, 44(5), 1308–1323, doi: 10.1109/Tgrs.2005.860986.  
 Couhert, A., T. Schneider, J. L. Li, D. E. Waliser, and A. M. Tompkins (2010), The maintenance of the relative humidity of the subtropical free troposphere, *J. Climate*, 23(2), 390–403, doi:10.1175/2009jcli2952.1.  
 Craig, H., and L. I. Gordon (1965), Deuterium and oxygen 18 variations in the ocean and the marine atmosphere, in *Stable Isotopes in Oceanographic Studies and Paleotemperatures*, edited by E. Tongiorgi, pp. 9–130, Lab. di Geol. Nucl., Pisa, Italy.  
 Dansgaard, W. (1964), Stable isotopes in precipitation, *Tellus*, 16(4), 436–468.  
 Ehhalt, D. H., F. Rohrer, and A. Fried (2005), Vertical profiles of HDO/H<sub>2</sub>O in the troposphere, *J. Geophys. Res.*, 110(D13), D13301, doi:10.1029/2004jd005569.  
 Field, R. D., D. B. A. Jones, and D. P. Brown (2010), The effects of post-condensation exchange on the isotopic composition of water in the atmosphere, *J. Geophys. Res. Atmospheres*, 115, D24305, doi:10.1029/2010JD014334.  
 Flanagan, L. B., J. P. Comstock, and J. R. Ehleringer (1991), Comparison of modeled and observed environmental influences on the stable oxygen and hydrogen isotope composition of leaf water in *Phaseolus vulgaris* L., *Plant Physiol.*, 96(2), 588–596.  
 Frankenberg, C., K. Yoshimura, T. Warneke, I. Aben, A. Butz, N. Deutscher, D. Griffith, F. Hase, J. Notholt, M. Schneider, H. Schrijver, and T. Rockmann (2009), Dynamic processes governing lower-tropospheric HDO/H<sub>2</sub>O ratios as observed from space and ground, *Science*, 325, 5946, doi:10.1126/Science.1173791.  
 Fu, R., B. Zhu, and R. E. Dickinson (1999), How do atmosphere and land surface influence seasonal changes of convection in the tropical amazon?, *J. Climate*, 12(5), 1306–1321.  
 Galewsky, J., and J. V. Hurley (2010), An advection-condensation model for subtropical water vapor isotopic ratios, *J. Geophys. Res.*, 115, D16116, doi:10.1029/2009jd013651.  
 Galewsky, J., A. Sobel, and I. Held (2005), Diagnosis of subtropical humidity dynamics using tracers of last saturation, *J. Atmos. Sci.*, 62(9), 3353–3367.  
 Gamache, J. F., and R. A. Houze (1983), Water-budget of a mesoscale convective system in the tropics, *J. Atmos. Sci.*, 40(7), 1835–1850.  
 Gedzelman, S., J. Lawrence, J. Gamache, M. Black, E. Hindman, R. Black, J. Dunion, H. Willoughby, and X. P. Zhang (2003), Probing hurricanes with stable isotopes of rain and water vapor, *Mon. Wea. Rev.*, 131(6), 1112–1127.  
 Grotes, P. M., M. Stuiver, L. G. Thompson, and E. Mosleythompson (1989), Oxygen isotope changes in tropical ice, Quelccaya, Peru, *J. Geophys. Res.*, 94(D1), 1187–1194.  
 Hendricks, M. B., D. J. DePaolo, and R. C. Cohen (2000), Space and time variation of  $\delta$  O-18 and  $\delta$  D in precipitation: Can paleotemperature be estimated from ice cores?, *Global Biogeochem. Cycles*, 14(3), 851–861.  
 Herbin, H., D. Hurtmans, S. Turquety, C. Wespes, B. Barret, J. Hadji-Lazaro, C. Clerbaux, and P. F. Coheur (2007), Global distributions of water vapour isotopologues retrieved from IMG/ADEOS data, *Atmos. Chem. Phys.*, 7(14), 3957–3968.  
 Huffman, G. J., R. F. Adler, B. Rudolf, U. Schneider, and P. R. Keehn (1995), Global precipitation estimates based on a technique for combining satellite-based estimates, rain-gauge analysis, and NWP model precipitation information, *J. Clim.*, 8(5), 1284–1295.



- Hurley, J. V., and J. Galewsky (2010), A last saturation analysis of ENSO humidity variability in the subtropical Pacific, *J. Climate*, 23(4), 918–931, doi:10.1175/2009jcli3193.1.
- IAEA/WMO. (2006), Global Network of Isotopes in Precipitation. The GNIP Database. (available at <http://isohis.iaea.org>).
- Jouzel, J., and L. Merlivat (1984), Deuterium and O-18 in precipitation—Modeling of the isotopic effects during snow formation, *J. Geophys. Res.*, 89, 1749–1757.
- Kalnay, E., M. Kanamitsu, R. Kistler, W. Collins, D. Deaven, L. Gandin, M. Iredell, S. Saha, G. White, J. Woollen, Y. Zhu, M. Chelliah, W. Ebisuzaki, W. Higgins, J. Janowiak, K. C. Mo, C. Ropelewski, J. Wang, A. Leetmaa, R. Reynolds, R. Jenne, and D. Joseph (1996), The NCEP/NCAR 40-year reanalysis project, *Bull. Am. Meteorol. Soc.*, 77(3), 437–471.
- Lawrence, J. R., and S. D. Gedzelman (1996), Low stable isotope ratios of tropical cyclone rains, *Geophys. Res. Lett.*, 23(5), 527–530.
- Lawrence, J. R., and S. D. Gedzelman (2003), Tropical ice core isotopes: Do they reflect changes in storm activity?, *Geophys. Res. Lett.*, 30(2), 1072–1076, doi:10.1029/2002gl015906.
- Lawrence, J. R., S. D. Gedzelman, D. Dexheimer, H. K. Cho, G. D. Carrie, R. Gasparini, C. R. Anderson, K. P. Bowman, and M. I. Biggerstaff (2004), Stable isotopic composition of water vapor in the tropics, *J. Geophys. Res.*, 109, D06115, doi:10.1029/2003jd004046.
- Lee, J., J. Worden, D. Noone, K. Bowman, A. Eldering, A. LeGrande, J. L. F. Li, G. Schmidt, and H. Sodemann (2011), Relating tropical ocean clouds to moist processes using water vapor isotope measurements, *Atmos. Chem. Phys.*, 11(2), 741–752, doi:10.5194/acp-11-741-2011.
- Lindzen, R. S., M. D. Chou, and A. Y. Hou (2001), Does the earth have an adaptive infrared iris?, *Bull. Am. Meteorol. Soc.*, 82(3), 417–432.
- Lossow, S., J. Steinwagner, J. Urban, E. Dupuy, C. D. Boone, S. Kellmann, A. Linden, M. Kiefer, U. Grabowski, N. Glatthor, M. Hopfner, T. Rockmann, D. P. Murtagh, K. A. Walker, P. F. Bernath, T. von Clarmann, and G. P. Stiller (2011), Comparison of HDO measurements from Envisat/MIPAS with observations by Odin/SMR and SCISAT/ACE-FTS, *Atmos. Measure. Techniq.*, 4, 9, doi:10.5194/amt-4-1855-2011.
- Mapes, B., J. Bacmeister, M. Khairoutdinov, C. Hannay, and M. Zhao (2009), Virtual field campaigns on deep tropical convection in climate models, *J. Climate*, 22(2), 244–257, doi:10.1175/2008jcli2203.1.
- Merlivat, L., and J. Jouzel (1979), Global climatic interpretation of the deuterium-oxygen-18 relationship for precipitation, *J. Geophys. Res.*, 84, 5029–5033.
- Noone, D. (2008), The influence of midlatitude and tropical overturning circulation on the isotopic composition of atmospheric water vapor and Antarctic precipitation, *J. Geophys. Res.*, 113, D04102, doi:10.1029/2007jd008892.
- Noone, D. (2012), Pairing measurements of the water vapor isotope ratio with humidity to deduce atmospheric moistening and dehydration in the tropical mid-troposphere, *J. Climate*, 25, 4476–4494, doi: 10.1175/JCLI-D-11-00582.1.
- Noone, D., and I. Simmonds (1999), A three-dimensional spherical trajectory algorithm, in Research Activities in Atmospheric and Oceanic Modelling, edited by H. Ritchie, pp. 3.26–3.27, World Meteorological Organization, Geneva, Switzerland.
- Noone, D., and C. Sturm (2010), Comprehensive dynamical models of global and regional water isotope distributions, in Isoscapes: Understanding Movement, Patterns, and Processes on Earth Through Isotope Mapping, edited by J. West, G. Bowen, T. Dawson and K. Tu, 487 pp., Springer, New York, N.Y.
- Noone, D., J. Galewsky, Z. D. Sharp, J. Worden, J. Barnes, D. Baer, A. Bailey, D. P. Brown, L. Christensen, E. Crosson, F. Dong, J. V. Hurley, L. R. Johnson, M. Strong, D. Toohey, A. Van Pelt, and J. S. Wright (2011), Properties of air mass mixing and humidity in the subtropics from measurements of the D/H isotope ratio of water vapor at the Mauna Loa Observatory, *J. Geophys. Res.*, 116, D22113, doi:10.1029/2011jd015773.
- Payne, V. H., D. Noone, A. Dudhia, C. Piccolo, and R. G. Grainger (2007), Global satellite measurements of HDO and implications for understanding the transport of water vapour into the stratosphere, *Q. J. R. Meteorol. Soc.*, 133(627), 1459–1471.
- Pierrehumbert, R. T. (1998), Lateral mixing as a source of subtropical water vapor, *Geophys. Res. Lett.*, 25(2), 151–154.
- Pierrehumbert, R. T. (1999), Subtropical water vapor as a mediator of rapid global climate change, *Geophys. Res. Lett.*, 112, 339–361.
- Risi, C., Bony, and F. Vimeux (2008), Influence of convective processes on the isotopic composition ( $\delta$  O-18 and  $\delta$  D) of precipitation and water vapor in the tropics: 2. Physical interpretation of the amount effect, *J. Geophys. Res.*, 113, D19306.
- Risi, C., D. Noone, J. Worden, C. Frankenberg, G. Stiller, M. Kiefer, B. Funke, K. Walker, P. Bernath, M. Schneider, S. Bony, J. Lee, D. Brown, and C. Sturm (2012a), Process-evaluation of tropospheric humidity simulated by general circulation models using water vapor isotopic observations: 2. Using isotopic diagnostics to understand the mid and upper tropospheric moist bias in the tropics and subtropics, *J. Geophys. Res.*, 117, D05304, doi:10.1029/2011jd016623.
- Risi, C., D. Noone, J. Worden, C. Frankenberg, G. Stiller, M. Kiefer, B. Funke, K. Walker, P. Bernath, M. Schneider, D. Wunch, V. Sherlock, N. Deutscher, D. Griffith, P. O. Wennberg, K. Strong, D. Smale, E. Mahieu, S. Barthlott, F. Hase, O. Garcia, J. Notholt, T. Warneke, G. Toon, D. Sayres, S. Bony, J. Lee, D. Brown, R. Uemura, and C. Sturm (2012b), Process-evaluation of tropospheric humidity simulated by general circulation models using water vapor isotopologues: 1. Comparison between models and observations, *J. Geophys. Res.*, 117, D05303, doi:10.1029/2011jd016621.
- Rozanski, K., L. Araguas-Araguas, and R. Gonfiantini (1992), Relation between long-term trends of O-18 isotope composition of precipitation and climate, *Science*, 258(5084), 981–985.
- Rozanski, K., L. Araguas-Araguas, and R. Gonfiantini (1993), Isotopic patterns in modern global precipitation, in Climate Change in Continental Isotopic Records, Geophys. Monogr. Ser., vol. 78, edited by P. K. Swart et al., pp. 1–36, AGU, Washington, D.C., doi:10.1029/GM078p0001.
- Schmidt, G. A., G. Hoffmann, D. T. Shindell, and Y. Y. Hu (2005), Modeling atmospheric stable water isotopes and the potential for constraining cloud processes and stratosphere-troposphere water exchange, *J. Geophys. Res.*, 110, D21314, doi:10.1029/2005jd005790.
- Shephard, M. W., R. L. Herman, B. M. Fisher, K. E. Cady-Pereira, S. A. Clough, V. H. Payne, D. N. Whiteman, J. P. Comer, H. Vomel, L. M. Miloshevich, R. Forno, M. Adam, G. B. Osterman, A. Eldering, J. R. Worden, L. R. Brown, H. M. Worden, S. S. Kulawik, D. M. Rider, A. Goldman, R. Beer, K. W. Bowman, C. D. Rodgers, M. Luo, C. P. Rinsland, M. Lampel, and M. R. Gunson (2008), Comparison of Tropospheric Emission Spectrometer nadir water vapor retrievals with in situ measurements, *J. Geophys. Res.*, 113, D15S24, doi:10.1029/2007jd008822.
- Sherwood, S. C. (1996), Maintenance of the free-tropospheric tropical water vapor distribution .2. Simulation by large-scale advection, *J. Climate*, 9(11), 2919–2934.
- Sherwood, S. C., R. Roca, T. M. Weckwerth, and N. G. Andronova (2010), Tropospheric water vapor, convection, and climate, *Rev. Geophys.*, 48, RG2001, doi:10.1029/2009rg000301.
- Steinwagner, J., M. Milz, T. von Clarmann, N. Glatthor, U. Grabowski, M. Hopfner, G. P. Stiller, and T. Rockmann (2007), HDO measurements with MIPAS, *Atmos. Chem. Phys.*, 7, 10.
- Still, C. J., W. J. Riley, S. C. Biraud, D. C. Noone, N. H. Buenning, J. T. Randerson, M. S. Torn, J. Welker, J. W. C. White, R. Vachon, G. D. Farquhar, and J. A. Berry (2009), Influence of clouds and diffuse radiation on ecosystem-atmosphere CO<sub>2</sub> and (COO)-O-18 exchanges, *J. Geophys. Res.*, 114, G01018, doi:10.1029/2007jg000675.
- Sun, D. Z., and R. S. Lindzen (1993), Distribution of tropical tropospheric water-vapor, *J. Atmos. Sci.*, 50(12), 1643–1660.
- Trenberth, K. E. (1999), Atmospheric moisture recycling: Role of advection and local evaporation, *J. Climate*, 12(5), 1368–1381.
- Trenberth, K. E., and C. J. Guillemot (1995), Evaluation of the global atmospheric moisture budget as seen from analyses, *J. Climate*, 8(9), 2255–2280.
- Trenberth, K. E., and C. J. Guillemot (1998), Evaluation of the atmospheric moisture and hydrological cycle in the NCEP/NCAR reanalyses, *Climate Dynam.*, 14(3), 213–231.
- Webster, C. R., and A. J. Heymsfield (2003), Water isotope ratios D/H, O-18/O-16, O-17/O-16 in and out of clouds map dehydration pathways, *Science*, 302, 1742–1745.
- Worden, J., S. S. Kulawik, M. W. Shephard, S. A. Clough, H. Worden, K. Bowman, and A. Goldman (2004), Predicted errors of tropospheric emission spectrometer nadir retrievals from spectral window selection, *J. Geophys. Res.*, 109(D9), D09308, doi:10.1029/2004jd004522.
- Worden, J., K. Bowman, D. Noone, R. Beer, S. Clough, A. Eldering, B. Fisher, A. Goldman, M. Gunson, R. Herman, S. S. Kulawik, M. Lampel, M. Luo, G. Osterman, C. Rinsland, C. Rodgers, S. Sander, M. Shephard, and H. Worden (2006), Tropospheric emission spectrometer observations of the tropospheric HDO/H<sub>2</sub>O ratio: Estimation approach and characterization, *J. Geophys. Res.*, 111, D16309.
- Worden, J., D. Noone, and K. Bowman (2007), Importance of rain evaporation and continental convection in the tropical water cycle, *Nature*, 445(7127), 528–532.
- Worden, J., D. Noone, J. Galewsky, A. Bailey, K. Bowman, D. Brown, J. Hurley, S. Kulawik, J. Lee, and M. Strong (2011), Estimate of bias in Aura TES HDO/H<sub>2</sub>O profiles from comparison of TES and in situ HDO/H<sub>2</sub>O measurements at the Mauna Loa Observatory, *Atmos. Chem. Phys.*, 11, 9, doi:10.5194/acp-11-4491-2011.
- Worden, J., S. Kulawik, C. Frankenberg, V. Payne, K. Bowman, K. Cady-Peirara, K. Wecht, J. E. Lee, and D. Noone (2012), Profiles of CH<sub>4</sub>, HDO, H<sub>2</sub>O, and N<sub>2</sub>O with improved lower tropospheric vertical resolution from Aura TES radiances, *Atmos. Measure. Techniq.*, 5, 2, doi:10.5194/amt-5-397-2012.

- Wright, J. S., R. Fu, and A. J. Heymsfield (2009a), A statistical analysis of the influence of deep convection on water vapor variability in the tropical upper troposphere, *Atmos. Chem. Phys.*, 9, 15, 5847–5864.
- Wright, J. S., A. H. Sobel, and G. A. Schmidt (2009b), Influence of condensate evaporation on water vapor and its stable isotopes in a GCM, *Geophys. Res. Lett.*, 36, L12804, doi:10.1029/2009gl038091.
- Wushiki, H. (1977), Deuterium content in the Himalayan precipitation at Khumbu District, observed in 1974/75, SEPPYO (Journal of the Japanese Society of snow and ice), 39 (Special Issue), 50–56.
- Yang, H., and R. T. Pierrehumbert (1994), Production of dry air by isentropic mixing, *J. Atmos. Sci.*, 51, 3437–3454, doi: [http://dx.doi.org/10.1175/1520-0469\(1994\)051<3437:PODABI>2.0.CO;2](http://dx.doi.org/10.1175/1520-0469(1994)051<3437:PODABI>2.0.CO;2).
- Zakharov, V. I., R. Imasu, K. G. Gribanov, G. Hoffmann, and J. Jouzel (2004), Latitudinal distribution of the deuterium to hydrogen ratio in the atmospheric water vapor retrieved from IMG/ADEOS data, *Geophys. Res. Lett.*, 31(12), L12104.